

Doping Mott Insulator in Ising-Kondo Lattice: Strange metal and Mott Criticality

Wei-Wei Yang,¹ Yin Zhong,^{1,*} and Hong-Gang Luo^{1,2}

¹*School of Physical Science and Technology & Key Laboratory for Magnetism and Magnetic Materials of the MoE, Lanzhou University, Lanzhou 730000, People Republic of China*

²*Beijing Computational Science Research Center, Beijing 100084, China*

(Dated: February 28, 2025)

Mottness as a key feature of strong electron correlation is most manifested in high- T_c cuprate superconductors, in which the strange metal (SM) behavior with linear- T dependence of resistivity has long been the major puzzle in condensed-matter physics. In this paper, we provide a numerically exact Monte Carlo study on a prototypical doped Mott insulator, i.e. the doped Ising-Kondo lattice (IKL) model. We find that the doping-driven Mott transition in IKL triggers a quantum critical region (QCR) with unexpected SM and quantum scaling behavior. Away from QCR, a robust non-Fermi liquid (NFL) state occupies most of regions above low- T magnetic ordered phases. The Luttinger theorem is unambiguously violated in SM and NFL, which is traced to anomalous c electron self-energy. The momentum and frequency dependence of self-energy around the Fermi energy is provided, with which the robust T -linear resistivity is accessible. Compared with the classic Hubbard model, our study suggests that SM and Mott quantum criticality are the intrinsic features of doped Mott insulator, which are promising to be revealed in generic strongly correlated electron systems.

The physics of high- T_c superconductors has long been taken as synonymous with that of the doped Mott insulator (MI). In doped cuprates, on the battle ground of MI and superconductivity, the normal state above optimal doped high- T_c cuprates superconductor exhibits unusual properties and is often referred to as the strange metal (SM) region. As a prototypical anomalous metal, the SM state with robust linear- T resistivity provides a major puzzle in condense matter physics despite of 30 years' effort.¹⁻¹⁰

model armed with dynamic-mean-field-theory (DMFT) reveal that the elusive SM behavior is caused by the doping-driven Mott quantum criticality^{11,12}. However, since non-local spatial fluctuation has been largely neglected in DMFT¹³⁻¹⁵ and merely Hubbard-like models have been carefully examined, some fundamental questions still remain open. Is the Mott quantum criticality together with the SM limited to the Hubbard model, or it is generic? Is it the result of approximation made in DMFT? Most of all, what is the characteristic microscopic signature of SM? Answering these questions is essential for deciphering the mechanism for SM and even the high- T_c superconductivity. Interestingly, a recent quantum Monte Carlo study suggests that the doped MI in the Hubbard model violates the Luttinger theorem, which signals the existence of non-Fermi liquid (NFL)¹⁶ beyond Landau's Fermi liquid (FL) paradigm¹⁷⁻¹⁹. Motivated by these important progresses and unsolved problems, we seek a clear and complete understanding about Mott criticality and SM behavior in an alternative model, which allows for nearly complete analytical and numerical treatment.

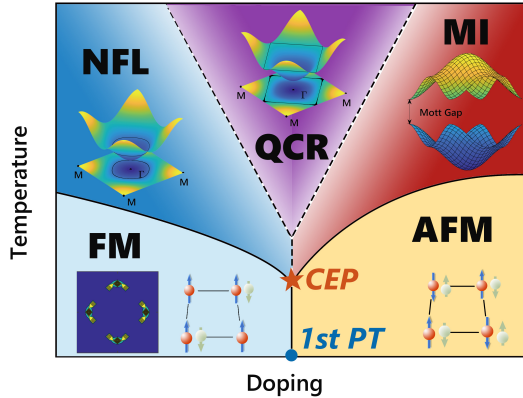


FIG. 1. Schematic phase diagram of the hole-doped Ising-Kondo lattice (IKL) model. The low temperature regime is divided into an antiferromagnetic insulator (AFMI) and a ferromagnetic metal (FMM) by a first-order transition, which transforms to a weak first-order transition and finally ends at the critical end point (CEP). At high temperature above CEP, a quantum critical region (QCR) is induced by doping-driven Mott insulator-metal transition, which displays the strange metal (SM) behavior. Out of QCR, there exists a Mott insulator (MI) at lower doping and a non-Fermi liquid (NFL) at a higher doping. Inset in MI shows two-band structure active at strong coupling while only lower band is depicted for QCR and NFL.

Fortunately, recent theoretical researches about Hubbard

We demonstrate the SM state in a doped MI modeled by Ising-Kondo lattice (IKL) model, with numerically exact Monte Carlo simulation technique, which establishes the intrinsic relation between Mott quantum criticality and the SM behavior. We remark IKL has been proposed to model f electron materials CeIrSn²⁰, TmB₄²¹ and hidden order compound URh₂Si₂²². A complete phase diagram is elaborated for the doped IKL, wherein the doping-driven Mott transition in IKL triggers a quantum critical region (QCR) with unexpected SM and quantum scaling behavior. Away from QCR, a robust NFL state occupies most of regions above low- T magnetic ordered phases (See Fig. 1). When comparing with existing literature on the Hubbard model, above findings are expected to be the generic features for doped MI. We believe our work opens a promising avenue to reveal Mott quantum criticality and SM behavior in more strongly correlated electron systems.

Model and Method.-We consider the IKL model on square

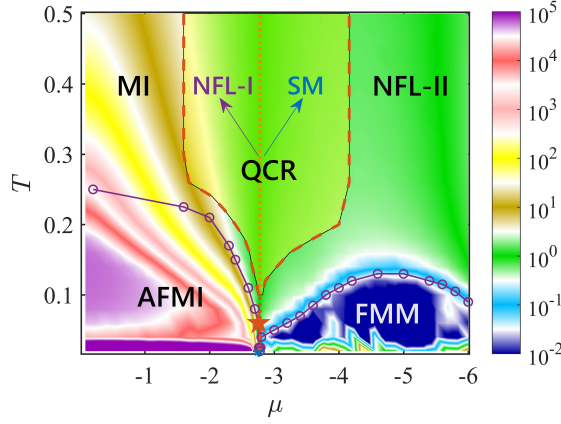


FIG. 2. Phase diagram of the doped IKL model on square lattice in $\mu - T$ plane with $J = 14$. Rich quantum states include AFMI, FMM, MI, insulator-like non-Fermi liquid (NFL-I), SM, and the second non-Fermi liquid (NFL-II). The background is a color map of the resistivity. Thermal fluctuation driven magnetic-paramagnetic phase transition is denoted by the purple line with circle mark. The first-order phase transition at ground state is marked by a blue circle. The quantum CEP is marked by a red pentagram. The QCR is delimited by the crossover temperature (red dashed line), which is characterized by the unusual scaling behavior. The metallic part of QCR is turned out to be SM, exhibiting linear- T dependent resistivity and logarithmic temperature dependence of the specific-heat coefficient. The separatrix line (red dash-dotted line) of QCR is around the minimum value of the error bar data in Monte Carlo (MC) simulation.

lattice whose Hamiltonian is defined as

$$\hat{H} = -t \sum_{i,j\sigma} \hat{c}_{i\sigma}^\dagger \hat{c}_{j\sigma} + \frac{J}{2} \sum_{j\sigma} \hat{S}_j^z \hat{c}_{j\sigma}^\dagger \hat{c}_{j\sigma} - \mu \sum_{j\sigma} \hat{c}_{j\sigma}^\dagger \hat{c}_{j\sigma}, \quad (1)$$

where $\hat{c}_{j\sigma}^\dagger$ ($\hat{c}_{j\sigma}$) is c electron's creation (annihilation) operator with spin $\sigma = \uparrow, \downarrow$ at site j . \hat{S}_j^z denotes the localized moment of f electron. t -term denotes the hopping integral and only nearest neighbor hopping is involved. The hole doping into the half-filled system ($\mu = 0$) is realized by tuning the chemical potential μ . J is the longitudinal Kondo coupling.

Choosing eigenstates of \hat{S}_j^z as basis, Eq. (H12) reduces into an effective free fermion model²³ under fixed background $\{q_j\}$, ($q_j = \pm 1$, $\hat{S}_j^z |q_j\rangle = \frac{q_j}{2} |q_j\rangle$) thus permits a straightforward classical (lattice) Monte Carlo simulation (see Supplementary Materials).

Monte Carlo simulations of IKL are carried out on the square lattice with periodic boundary conditions, where a 20×20 square lattice is mainly used. Accordingly, the two-dimensional Brillouin zone are sampled by a 20×20 k -point grid. Nearest neighbor hopping integral is used as the unit ($t = 1$) to measure all energy scales. To attack the Mottness, we focus on the strong coupling regime ($J = 14$).

Phase Diagram.—Our main result about the doped IKL is summarized in the $\mu - T$ phase diagram (see Fig. 11), where the color bar denotes resistivity scaled by the one in separatrix line (dotted line) of the QCR. (see $n_c - T$ phase diagram

in Supplementary Materials) The competition between itinerant and local tendency leads to different magnetic order, and thus conspire to construct rich quantum states in IKL, including antiferromagnetic insulator (AFMI), ferromagnetic metal (FMM) at low temperature and paramagnetic phases as MI, SM, NFL at high temperature. (see Supplementary Materials for low- T magnetic states) The magnetic-paramagnetic phase transition (Fig. 11, purple line with circle) is determined by the peak in heat capacity (see Fig. 14a) and belongs to the two-dimensional Ising universality class, which is similar to the half-filled IKL²³. There exists a critical end point (CEP, see the red pentagram in Fig. 11), below which a first-order phase transition separates the IKL system into AFMI and FMM. Above CEP, QCR is uncovered, whose resistivity satisfies the following quantum critical scaling (see Fig. 3)

$$\rho(T, \delta\mu) = \rho^*(T) f(T/T_0(\delta\mu)), \quad (2)$$

where $T_0(\delta\mu) = c|\delta\mu|^{z\nu}$, $\delta\mu = \mu - \mu^*(T)$ and $\mu^*(T)$ is the critical 'zero field' trajectory corresponding to the 'separatrix' line²⁴. $\rho^*(T)$ is calculated for $\mu = \mu^*(T)$ and $f(x)$ denotes the unknown scaling function. The resistivity on the separatrix is almost independent with temperature. Note that at high temperatures, the resistivity curves depend weakly on different parameter, while as temperature is reduced the critical line separates resistivity curves to two branches. Here, we refer the insulator-like branch to the first non-Fermi liquid state (NFL-I)²⁵ and the metallic one to SM, respectively. The resistivity curves display the bifurcating characteristic. Crossing the center line, there is a change in trend with varying temperature. Both branches display the power-law scaling $T_0(\delta\mu) = c|\delta\mu|^{z\nu}$ with the same exponents $z\nu = 1.25$, and the $T_0(\delta\mu)$ do vanish as $\delta\mu \rightarrow 0$, indicating a quantum criticality instead of classical phase transition²⁶.

As shown in Fig. 3, the scaling function displays mirror symmetry over almost two decades ($10^0 \sim 10^2$) in T/T_0 . Apart from the resistivity, other physical quantities such as heat capacity and the magnetic susceptibility also display the quantum scaling behaviors. (These results are crosschecked by a DMFT study, see Supplementary Materials) Out of QCR, we dub the NFL state without quantum scaling behavior as the second non-Fermi liquid (NFL-II)²⁵.

strange-metal state.—To locate SM^{5,6}, we first examine the heat capacity $C(T)$ and resistivity $\rho(T)$ at various doping. In Fig. 14 we plot the evolution of both thermal and transport properties with varying doping in Fig. 14b,c. With decreasing temperature, in SM the heat capacity coefficient $C(T)/T$ increases with decreasing temperature, exhibiting an obvious dependence proportional to $-\log(T)$ before approaching the magnetic phase transition. In Fig. 14c we demonstrate the resistivity in QCR, which demonstrates a power-law dependence of temperature, satisfying $\rho(T) = \rho_0 + AT^n$ and the n gradually changes from 2 to 1. In SM, an obvious linear- T dependence is revealed.

Violation of Luttinger theorem.—Next, we examine whether the Luttinger theorem satisfied by FL is obeyed by SM. The Luttinger theorem^{27,28} states that for generic FL states the Luttinger integral (IL) below equals to density of particles

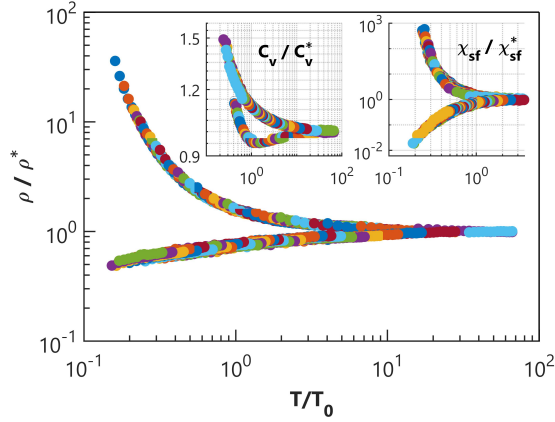


FIG. 3. Unconventional scaling behavior of resistivity in the QCR. Family of resistivity curves are calculated along lines parallel to the separatrix $\mu^*(T)$ and is rescaled in the formula $\rho(T, \delta\mu)/\rho^*(T) = f(T/T_0(\delta\mu))$. At high temperature the resistivity depends weakly on the doping parameter. With decreasing temperature the curves demonstrate the bifurcating characteristic, which is separated into an insulator-like one and a metallic one. Both branches satisfy the same power-law scaling $T_0(\delta\mu) = c|\delta\mu|^{z\nu}$ with $z\nu = 1.25$, indicating the quantum criticality in the QCR. Inset plots the scaling behavior of thermodynamical properties, e.g., heat capacity C_V of c electron and the susceptibility of f electron χ_{sf} . The critical exponent is different for the f electrons, where $(z\nu)_f = 0.55$.

(n_c)

$$\text{IL} = \sum_{\sigma} \int_{\theta(\text{Re}G(\mathbf{k}, 0))} \frac{d^d k}{(2\pi)^d}. \quad (3)$$

Figure. 16 demonstrates the seriously violated Luttinger theorem at strong coupling ($J = 14$, $\text{IL} \sim 2n_c$). It suggests a robust NFL-like nature for all paramagnetic phases in the phase diagram (see Fig. 11), including SM. On the contrary, the Luttinger theorem works well in the weak coupling case ($J = 2$), agreeing with its FL nature. Extra features in Fig. 16 is that the IL shows two incipient divergences when approaching the boundary of QCR. One divergence occurs around $\mu = -1.6$ ($T = 0.3, n_c \sim 0.96$; $T = 0.4, n_c \sim 0.93$; $T = 0.5, n_c \sim 0.91$), suggesting the Mott insulator-metal transition. The Mott transition is a third-order doping-driven phase transition, which is also indicated by the maximum of $\frac{\partial^2 n_c}{\partial \mu^2}$. Another divergence occurs around $\mu = -3.6$ ($n_c \sim 0.53$), which is also close to the edge of QCR.

To get further insight into the violation of Luttinger theorem, the electron's spectral function ($A_{\mathbf{k}}(\omega = 0)$) and the real part of Green function $\text{Re}G(\mathbf{k}, 0)$ at the Fermi energy are carefully studied (see Fig. 17). The electron density is marked by the size of the Luttinger contour in a free system (white line). We compare the situation in FL (left panel), SM (middle panel) and NFL-II (right panel). The FL has a Luttinger-volume Fermi surface, where the volume enclosed by the Fermi surface is consistent with the Luttinger contour ($n_c = 0.36$). To the contrary, both the SM ($n_c = 0.67$) and NFL-II ($n_c = 0.31$) states display a non-Luttinger-volume Fermi surface, underly-

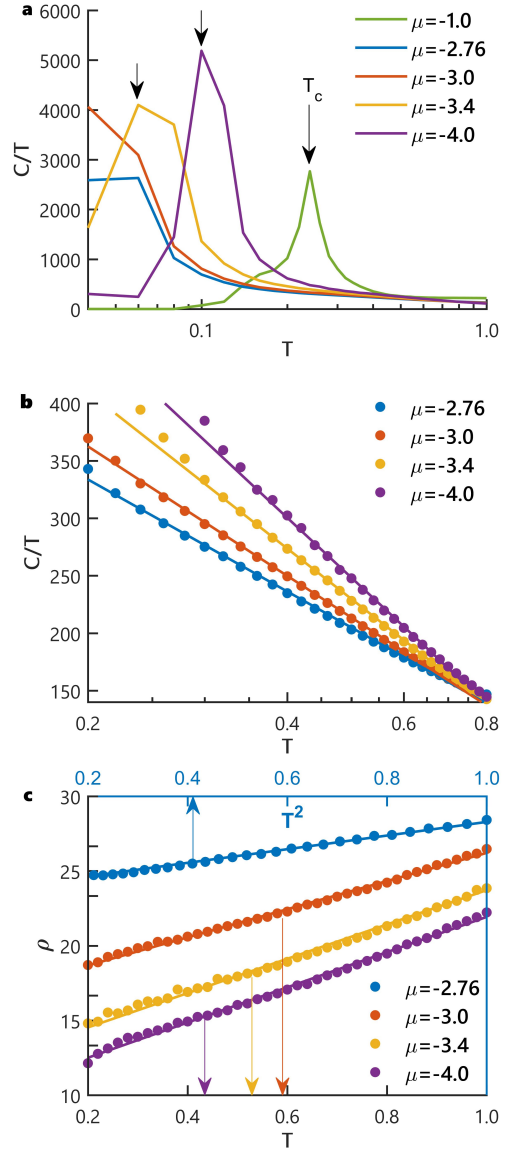


FIG. 4. Anomalous transport and thermodynamics in the SM. **a**, Specific heat under different doping. The peak position corresponds to T_c of magnetic-paramagnetic phase transition. **b**, The same plot of specific heat with the y-axis magnified in the paramagnetic region. The solid line is fitted by a $\log T$ function. In SM, $C(T)/T$ exhibits logarithm temperature dependence. **c**, Resistivity under different doping in the QCR. In QCR $\rho(T)$ satisfies a power-law dependence of temperature ($\rho(T) = \rho_0 + AT^n$). With increasing doping, the resistivity changes from T^2 -dependent behavior ($\mu = -2.76$) to a linear- T dependence ($\mu = -3.0, -3.4, -4.0$), indicating the SM behavior.

ing a robust NFL behavior in the paramagnetic regime of the doped IKL.

Microscopic mechanism underlying SM behaviors.-Finally, we turn our attention to microscopic mechanism underlying SM behaviors. Technically, we can extract electron's self-energy $\Sigma(\mathbf{k}, \omega)$ via Dyson equation. In Fig. 18 we plot the real and imaginary part of self-energy at Fermi energy and

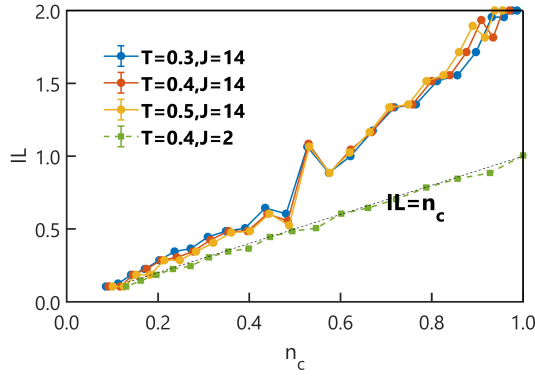


FIG. 5. Luttinger integral (IL) versus density of electron n_c . In FL ($J = 2$), the electron density is accordance with the Luttinger theorem. At strong coupling ($J = 14$), IL strongly deviates from the density of electrons for most doping regime thus confirms their NFL nature. At high temperature, IL diverges close to the boundary of QCR.

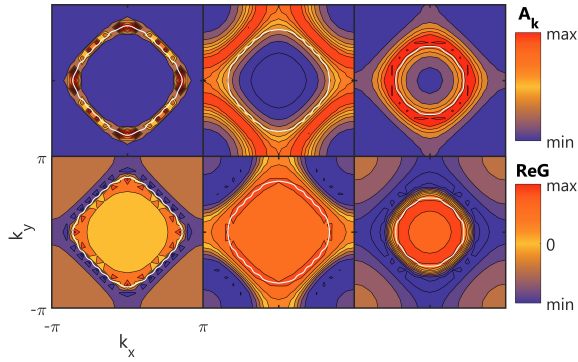


FIG. 6. Spectral function at Fermi energy $A_k(\omega = 0)$ (upper panel) and real part of Green function at Fermi energy $\text{Re}G(\mathbf{k}, 0)$ (lower panel) in different high-temperature phases: FL (left panel, $J = 2$, $T = 0.4$, $\mu = -0.8$); SM ($J = 14$, $T = 0.4$, $\mu = -3.0$, middle panel); NFL-II ($J = 14$, $T = 0.4$, $\mu = -4.6$, right panel). The electron density is denoted by the Luttinger contour (white circle). The maximum of spectral function corresponds to Fermi surface. In FL state both $A_k(\omega = 0)$ and $\text{Re}G(\mathbf{k}, 0)$ diverge at the Fermi surface, while in the SM and NFL-II states $\text{Re}G(\mathbf{k}, 0)$ changes smoothly at the Fermi surface.

investigate its momentum dependence around the Fermi surface for the SM. As reference, the momentum dependence of FL ($J = 2, T = 0.4$) around Fermi surface is displayed in Fig. 18b. The Fermi surface is demonstrated in Fig. 18a and the momentum is chosen along the dotted line. In FL, the real part of self-energy displays a linear k -dependent behavior, while the imaginary part displays a k^2 -dependent behavior. In contrast, SM ($J = 14, \mu = -3.0, T = 1.0$) and NFL ($J = 14, \mu = -4.6, T = 1.0$) show distinct form, where both real and imaginary part demonstrate linear-momentum dependence $\text{Re}\Sigma(\omega = 0) \sim k - k_F$, $\text{Im}\Sigma(\omega = 0) \sim k - k_F$.

The frequency dependence of self-energy around Fermi energy is shown in Fig. 8, where the data is fitted with $\Sigma(\omega) \sim$

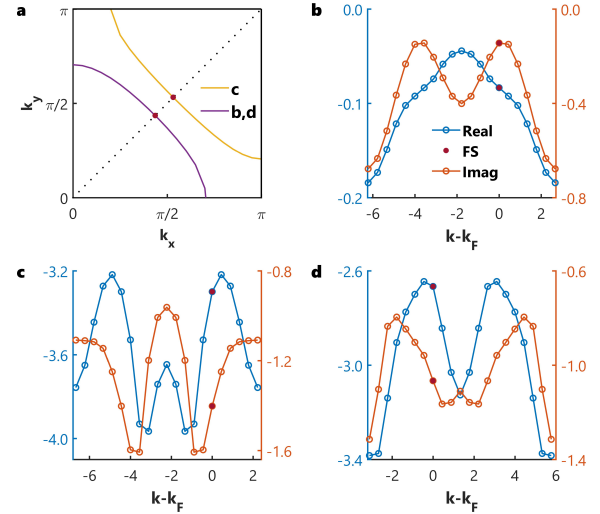


FIG. 7. Momentum dependence to the self-energy calculated around the Fermi energy. **a**, Schematic picture for the Fermi surface in **b-d**. In **b** and **d**, Fermi surface (purple line) coincides with each other, whereas the electron density in FL (IL = 0.72) is double the one in NFL-II (IL = 0.36). The self-energy is calculated along the black dotted line and the position of Fermi surface is marked with the red circle. **b-d**, Momentum dependence to the self-energy in FL state (**b**, $J = 2, T = 0.4, \mu = -0.8$), SM (**c**, $J = 14, T = 1, \mu = -3.0$) and NFL-II (**d**, $J = 14, T = 1, \mu = -4.6$). In FL, the real part of the self-energy demonstrates a linear dependence of momentum, while the imaginary part shows a quadratic dependence, i.e., $\text{Re}\Sigma(\omega = 0) \sim k - k_F$ and $\text{Im}\Sigma(\omega = 0) \sim (k - k_F)^2$. In contrast, the SM and NFL-II states display a linear momentum dependence for both the real and imaginary part of self-energy, $\text{Re}\Sigma(\omega = 0) \sim k - k_F$ and $\text{Im}\Sigma(\omega = 0) \sim k - k_F$.

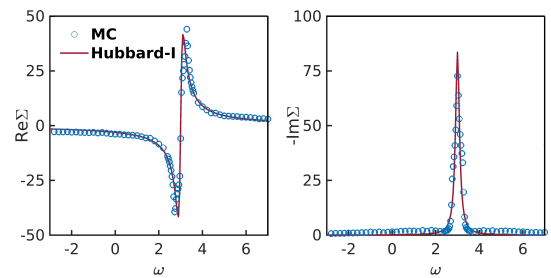


FIG. 8. Frequency dependence of self-energy in SM ($\mu = -3.0, T = 1.0$). The result of Hubbard-I approximation valid at strong coupling limit is displayed (red line), and it is in good agreement with MC result (blue circle).

$\frac{J^2/16}{\omega + \mu + i\Gamma}$ inspired by analytic Hubbard-I approximation²³. Thus in NFL/SM, the self-energy at the Fermi energy is approximately given by

$$\Sigma(\mathbf{k}, \omega) = a \frac{J^2/16}{\omega + \mu + i\Gamma} + b(\mathbf{k} - \mathbf{k}_F), \quad (4)$$

where \mathbf{k}_F is the Fermi momentum. The fitting coefficient a and Γ under different coupling strength are provided in tabel.I,

indicating a similar frequency dependence of the self-energy under strong coupling. Previous study on the Hubbard and Sachdev-Ye-Kitaev models has attributed the T -linear resistivity to the broadening of spectral function by a T -independent scattering rate²⁹. Since in the doped IKL the two-peaked spectral function is robust versus varying temperature at paramagnetic region, with the coefficient in table.I we calculate the resistivity by the Kubo formula

$$\sigma_{DC} = 2\pi \int d\epsilon \phi(\epsilon) \int \frac{\beta d\omega A(\epsilon, \omega)^2}{4 \cosh^2(\beta\omega/2)}. \quad (5)$$

As shown in Fig. 9, a clear linear- T dependence is demonstrated for all coupling strength. Therefore, we conclude that our system accesses to robust linear- T resistivity with the self-energy in the form of Eq. 4.

TABLE I. Fitting coefficient of the frequency dependence of self-energy with varying coupling strength.

	$J = 12$	$J = 14$	$J = 16$	$J = 18$
a	0.7	0.75	0.85	0.85
Γ	0.15	0.11	0.07	0.07

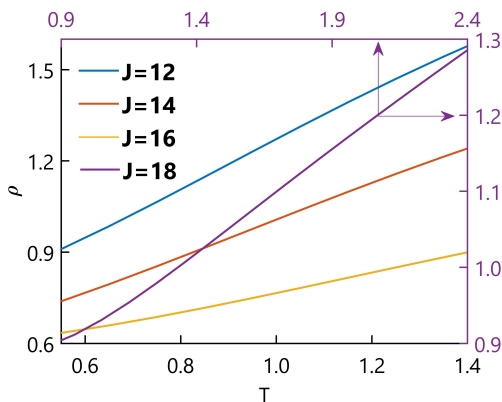


FIG. 9. Resistivity as a function of temperature, calculated with the fitting coefficient in tabel.I, where robust linear- T dependence is revealed.

Discussion and conclusion.-We remark that a similar phase diagram like Fig. 11 has been reported in the Hubbard model with the DMFT approximation^{11,12}. Comparing the anomalous phenomenon in the IKL and the Hubbard model, we find these two models share several common properties around Mott insulator-metal transition as following. (i) A robust NFL state is revealed around the transition with a linear- T resistivity (e.g., Fig. 14c). (ii) The Mott transition is turned out to be third-order, indicated by the divergence of $\frac{\partial^2 n_c}{\partial \mu^2}$. (iii) Resistivity satisfies a quantum critical scaling like Eq. 2 with similar critical exponent ($(z\nu)_{IKL} = 1.25$, $(z\nu)_{Hubbard} = 1.35$).

There also exist some differences. The doped MI in the IKL has rigid band while in the Hubbard model spectral-weight transfer leads to non-rigid band. Furthermore, IKL

has magnetic ordered states at low temperature, but such magnetic solutions in the Hubbard model are suppressed in DMFT though the true low-temperature states are unknown. When approaching battleground of multiple low-temperature competing orders, both quantum critical point and the QCR behavior might be in the danger of destruction. Fortunately, Monte Carlo simulation in IKL includes both local and nonlocal correlation, thus provides a solid platform to investigate the Mott quantum criticality.

Comparing IKL to solvable doped Mott insulator in Hastugai-Kohmoto (HK) model,³⁰ one see that no Luttinger surface exists in IKL (also in SYK and Hubbard) while HK supports robust Luttinger surface characterized by zeros of Green function. Thus, the Luttinger surface may not be generic feature for doped MI though it kills FL.

In conclusion, by studying a numerically solvable doped MI, a doping-driven Mott insulator-metal transition is revealed, accompanied with SM behavior and quantum critical scaling. The Luttinger theorem is unambiguously violated in this doped MI as a result of anomalous electron self-energy. The self-energy at low energy provides an explanation for the robust linear- T resistivity observed in SM state. Compared with the classic Hubbard model, our study suggests that SM, Mott quantum criticality and the presence of Fermi surface with NFL-like self-energy are the intrinsic features of doped MI, which are promising to be revealed in generic strongly correlated electron systems.

ACKNOWLEDGMENTS

This research was supported in part by Supercomputing Center of Lanzhou University and NSFC under Grant No. 11704166, No. 11834005, No. 11874188, No. 11674139. We thank the Supercomputing Center of Lanzhou University for allocation of CPU time.

Appendix A: detail of Lattice Monte Carlo simulation

When exploring the finite temperature properties, one has to sum over all configurations of effective Ising spin q_j , which can only be performed via Monte Carlo simulation.

1. Monte Carlo simulation

Firstly, we know that the equilibrium state thermodynamics is controlled by the partition function

$$\mathcal{Z} = \text{Tr} e^{-\beta \hat{H}} = \text{Tr}_c \text{Tr}_S e^{-\beta \hat{H}} = \sum_{\{q_j\}} \text{Tr}_c e^{-\beta \hat{H}(q)}. \quad (A1)$$

Here, the trace is split into c -fermion and \hat{S}^z , where the latter is transformed into the summation over all possible configuration $\{q_j\}$. For each single-particle Hamiltonian $\hat{H}(q)$, it can be

easily diagonalized into

$$\hat{H}(q) = \sum_n E_n \hat{d}_n^\dagger \hat{d}_n, \quad (\text{A2})$$

where E_n is the single-particle energy level and \hat{d}_n is the quasi-particle. The fermion \hat{d}_n is related into \hat{c}_j via

$$\hat{c}_j = |0\rangle\langle j| = \sum_n |0\rangle\langle j|n\rangle\langle n| = \sum_n |0\rangle\langle n|j\rangle\langle n| = \sum_n \hat{d}_n \phi_n^j, \quad (\text{A3})$$

with $\phi_n^j \equiv \langle j|n\rangle$ while the creation operator \hat{c}^\dagger has

$$\hat{c}^\dagger = |j\rangle\langle 0| = \sum_n |n\rangle\langle n|j\rangle\langle 0| = \sum_n |n\rangle\langle 0|n\rangle\langle j| = \sum_n \hat{d}_n^\dagger (\phi_n^j)^*. \quad (\text{A4})$$

Now, the trace over c -fermion can be obtained as

$$\begin{aligned} \text{Tr} e^{-\beta \hat{H}} &= \sum_n \langle n | e^{-\beta \sum_m E_m \hat{d}_m^\dagger \hat{d}_m} | n \rangle \\ &= \prod_m \sum_n \langle n | e^{-\beta E_m \hat{d}_m^\dagger \hat{d}_m} | n \rangle \\ &= \prod_m \sum_n \sum_{n_m=0,1} \delta_{n,m} (1 + e^{-\beta E_m n_m}) \\ &= \prod_m \sum_n \delta_{n,m} (1 + e^{-\beta E_m}) \\ &= \prod_m (1 + e^{-\beta E_m}). \end{aligned} \quad (\text{A5})$$

This is the familiar result for free fermion, however one should keep in mind that E_n actually depends on the effective Ising spin configuration $\{q_j\}$, thus we write $E_n(q)$ to emphasize this fact.

So, the partition function reads

$$\mathcal{Z} = \sum_{\{q_j\}} \prod_n (1 + e^{-\beta E_n(q)}) = \sum_{\{q_j\}} e^{-\beta F(q)}, \quad (\text{A6})$$

where we have defined an effective free energy

$$F(q) = -T \sum_n \ln(1 + e^{-\beta E_n(q)}). \quad (\text{A7})$$

In this situation, we can explain $e^{-\beta F(q)}$ or $\rho(q) = \frac{1}{\mathcal{Z}} e^{-\beta F(q)}$ as an effective Boltzmann weight for each configuration of $\{q_j\}$ and this can be used to perform Monte Carlo simulation just like the classic Ising model. Specifically, we start with random or chosen configuration of $\{q_j\}$, then try to flip each q_j to $-q_j$. The relative probability for such flip is determined by effective Boltzmann weight

$$r = \frac{e^{-\beta F_{new}(q)}}{e^{-\beta F_{old}(q)}} = e^{-\beta(F_{new}(q) - F_{old}(q))}, \quad (\text{A8})$$

where $F_{old}(q)$, $F_{new}(q)$ denotes the effective free energy before and after flip. This is the weight used in the classic Metropolis importance sampling. Alternatively, one can use the so-called bath algorithm, which means

$$r = \frac{r}{1+r}, \quad (\text{A9})$$

such that the probability is seemingly normalized. Then, we generate a random number a from uniform distribution $[0, 1]$ and compare this with \tilde{r} . If $\tilde{r} > a$, the flip of q_j is accepted and F_{old} is updated into F_{new} , otherwise we reset q_j to its original value before the flip. By trying to flip q_j over all sites, this is called a sweep and doing such sweep many times, the system can be equilibrium and the next sweeps are used to calculate physical observable.

2. on physical quantities

To calculate physical quantities, we consider generic operator \hat{O} , which can be split into part with only Ising spin $\{q_j\}$ and another part with fermions,

$$\hat{O} = \hat{O}^c + \hat{O}^q. \quad (\text{A10})$$

Then, its expectation value in the equilibrium ensemble reads

$$\langle \hat{O} \rangle = \langle \hat{O}^c \rangle + \langle \hat{O}^q \rangle = \frac{\text{Tr} \hat{O}^c e^{-\beta \hat{H}}}{\text{Tr} e^{-\beta \hat{H}}} + \frac{\text{Tr} \hat{O}^q e^{-\beta \hat{H}}}{\text{Tr} e^{-\beta \hat{H}}}. \quad (\text{A11})$$

For \hat{O}^q , we have

$$\begin{aligned} \langle \hat{O}^q \rangle &= \frac{\sum_{\{q_j\}} \hat{O}^q(q) e^{\beta h \sum_j q_j} \text{Tr}_c e^{-\beta \hat{H}(q)}}{\sum_{\{q_j\}} e^{-\beta F(q)}} \\ &= \frac{\sum_{\{q_j\}} \hat{O}^q(q) e^{-\beta F(q)}}{\sum_{\{q_j\}} e^{-\beta F(q)}} \\ &= \sum_{\{q_j\}} \hat{O}^q(q) \rho(q). \end{aligned} \quad (\text{A12})$$

In the Metropolis importance sampling algorithm, the above equation means we can use the simple average to estimate the expectation value like

$$\langle \hat{O}^q \rangle \simeq \frac{1}{N_m} \sum_{\{q_j\}} \hat{O}^q(q), \quad (\text{A13})$$

where N_m is the number of sampling and the sum is over each configuration. $\hat{O}^q(q)$ is a number since we always work on the basis of $\{q_j\}$.

For \hat{O}^c ,

$$\langle \hat{O}^c \rangle = \frac{\sum_{\{q_j\}} e^{\beta h \sum_j q_j} \text{Tr}_c \hat{O}^c(q) e^{-\beta \hat{H}(q)}}{\sum_{\{q_j\}} \text{Tr}_c e^{-\beta \hat{H}(q)}} \quad (\text{A14})$$

and we can insert $\frac{e^{-\beta F(q)}}{e^{-\beta F(q)}}$ in the numerator, which leads to

$$\begin{aligned} \langle \hat{O}^c \rangle &= \sum_{\{q_j\}} \frac{\text{Tr}_c \hat{O}^c(q) e^{-\beta \hat{H}(q)}}{\text{Tr}_c e^{-\beta \hat{H}(q)}} \frac{e^{-\beta F(q)}}{\sum_{\{q_j\}} e^{-\beta F(q)}} \\ &= \sum_{\{q_j\}} \frac{\text{Tr}_c \hat{O}^c(q) e^{-\beta \hat{H}(q)}}{\text{Tr}_c e^{-\beta \hat{H}(q)}} \rho(q) \\ &= \sum_{\{q_j\}} \langle \langle \hat{O}^c \rangle \rangle \rho(q). \end{aligned} \quad (\text{A15})$$

This means

$$\langle \hat{O}^c \rangle \simeq \frac{1}{N_m} \sum_{\{q_j\}} \langle \langle \hat{O}^c(q) \rangle \rangle, \quad (\text{A16})$$

where $\langle \langle \hat{O}^c(q) \rangle \rangle = \frac{\text{Tr}_c \hat{O}^c e^{-\beta \hat{H}(q)}}{\text{Tr}_c e^{-\beta \hat{H}(q)}}$ is calculated based on Hamiltonian $\hat{H}(q)$. More practically, such statement means if fermions are involved, one can just calculate with $\hat{H}(q)$. Then, average over all sampled configuration gives rise to the wanted results.

3. Energy, correlation and others

The total energy of our system is an essential quantity and can be calculated as

$$\begin{aligned} \langle \hat{H} \rangle &\simeq \frac{1}{N_m} \sum_{\{q_j\}} [\langle \langle \hat{H}(q) \rangle \rangle] \\ &= \frac{1}{N_m} \sum_{\{q_j\}} \left[\sum_n E_n(q) f_F(E_n(q)) \right]. \end{aligned} \quad (\text{A17})$$

Here, the $\langle \langle \hat{H}(q) \rangle \rangle$ is just the summation over all quasiparticles for given configuration. Now, the specific heat C_v can be found by $C_v = \frac{\langle \hat{H}^2 \rangle - \langle \hat{H} \rangle^2}{T^2}$, which means

$$C_v \simeq \frac{\frac{1}{N_m} \sum_{\{q_j\}} \langle \langle \hat{H}^2(q) \rangle \rangle}{T^2} - \frac{\langle \hat{H} \rangle^2}{T^2}, \quad (\text{A18})$$

where

$$\begin{aligned} \langle \langle \hat{H}^2(q) \rangle \rangle &= \left(\sum_n E_n(q) f_F(E_n(q)) \right)^2 \\ &+ \sum_n E_n^2(q) f_F(E_n(q)) [1 - f_F(E_n(q))]. \end{aligned} \quad (\text{A19})$$

Next, we consider the spin-spin correlation function $S_{qq}(Q)$, which is defined as

$$S_{qq}(Q) = \frac{1}{N_s^2} \sum_{ij} e^{iQ(R_i - R_j)} \langle q_i q_j \rangle. \quad (\text{A20})$$

This object is designed to detect the static or dynamic (fluctuation) order with the characteristic wave-vector Q . If spin orders in certain Q , the value of the corresponding $S_{qq}(Q)$ should reach $O(1)$. Now, using Eq. A13, we obtain

$$S_{qq}(Q) \simeq \frac{1}{N_m} \sum_{\{q_j\}} \left[\frac{1}{N_s^2} \sum_{ij} e^{iQ(R_i - R_j)} q_i q_j \right]. \quad (\text{A21})$$

Usually, we may also use its susceptibility

$$\begin{aligned} \chi_{qq}(Q) &= \frac{\langle S_{qq}^2(Q) \rangle - \langle S_{qq}(Q) \rangle^2}{T} \\ &\simeq \frac{1}{T} \frac{1}{N_m} \sum_{\{q_j\}} \left[\frac{1}{N_s^2} \sum_{ij} e^{iQ(R_i - R_j)} q_i q_j \right]^2 \\ &- \frac{1}{T} \left(\frac{1}{N_m} \sum_{\{q_j\}} \left[\frac{1}{N_s^2} \sum_{ij} e^{iQ(R_i - R_j)} q_i q_j \right] \right)^2 \end{aligned} \quad (\text{A22})$$

to locate the position of long-ranged order. Obviously, if orders appear, $\chi_{qq}(Q)$ has to diverge for certain Q at some critical temperature T_c . At T_c , the specific heat C_v diverges as well.

For total c electron density, in term of Eq. A16, it is easy to show that

$$n_c = \frac{1}{N_s} \sum_j \langle \hat{c}_j^\dagger \hat{c}_j \rangle \simeq \frac{1}{N_m} \sum_{\{q_j\}} \left[\frac{1}{N_s} \sum_n f_F(E_n(q)) \right]. \quad (\text{A23})$$

Since we work on grand canonical ensemble, if chemical potential is setting as zero, the model is symmetric and c electron should be half-filled. Thus, in this situation $n_c = 1$, irrespective of temperature.

If we are interested in the DOS $N(\omega)$ of c electron, we know that for $\hat{H}(q)$, it is given by

$$N(\omega, q) = \frac{1}{N_s} \sum_n \delta(\omega - E_n(q)), \quad (\text{A24})$$

thus,

$$N(\omega) \simeq \frac{1}{N_m N_s} \sum_{\{q_j\}} \sum_n \delta(\omega - E_n(q)). \quad (\text{A25})$$

Finally, when we calculate fermion's correlation function like $\langle \hat{c}_i^\dagger \hat{c}_j \hat{c}_k^\dagger \hat{c}_l \rangle$,

$$\langle \hat{c}_i^\dagger \hat{c}_j \hat{c}_k^\dagger \hat{c}_l \rangle = \frac{1}{N_m} \sum_{\{q_j\}} \langle \langle \hat{c}_i^\dagger \hat{c}_j \hat{c}_k^\dagger \hat{c}_l \rangle \rangle. \quad (\text{A26})$$

Then, using the Wick theorem for these free fermions, we get

$$\langle \langle \hat{c}_i^\dagger \hat{c}_j \hat{c}_k^\dagger \hat{c}_l \rangle \rangle = \langle \langle \hat{c}_i^\dagger \hat{c}_j \rangle \rangle \langle \langle \hat{c}_k^\dagger \hat{c}_l \rangle \rangle + \langle \langle \hat{c}_i^\dagger \hat{c}_l \rangle \rangle \langle \langle \hat{c}_j \hat{c}_k^\dagger \rangle \rangle. \quad (\text{A27})$$

Next, for each one-body correlation function like $\langle \langle \hat{c}_i^\dagger \hat{c}_j \rangle \rangle$, one can transform these objects into their quasiparticle basis,

$$\begin{aligned} g_{ij}^q &\equiv \langle \langle \hat{c}_i^\dagger \hat{c}_j \rangle \rangle = \sum_{m,n} \langle \langle \hat{d}_m^\dagger \hat{d}_n \rangle \rangle (\phi_m^i)^* \phi_n^j \\ &= \sum_{m,n} f_F(E_n(q)) \delta_{n,m} (\phi_m^i)^* \phi_n^j \\ &= \sum_n f_F(E_n(q)) (\phi_n^i)^* \phi_n^j. \end{aligned} \quad (\text{A28})$$

Similarly, we have

$$\langle \langle \hat{c}_i \hat{c}_j^\dagger \rangle \rangle = \sum_n (1 - f_F(E_n(q))) \phi_n^i (\phi_n^j)^* = \delta_{ij} - g_{ji}^q. \quad (\text{A29})$$

Then, combining Eq. A27 and inserting this expression into the Eq. A26, we can calculate the fermion's correlation function.

For instance, the spin-density-wave structure factor is calculated as

$$\begin{aligned}
C_{\text{SDW}} &= \frac{1}{N_m} \sum_{\{q_j\}} \frac{1}{4N_s^2} \sum_{j,k,\sigma,\sigma'} (-1)^{j+k} \\
&\times \langle\langle (\sigma \hat{c}_{j\sigma}^\dagger \hat{c}_{j\sigma}) (\sigma' \hat{c}_{k\sigma'}^\dagger \hat{c}_{k\sigma'}) \rangle\rangle \\
&= \frac{1}{N_m} \sum_{\{q_j\}} \frac{1}{4N_s^2} \sum_{j,k} (-1)^{j+k} \times [g_{jj,\uparrow}^q g_{kk,\uparrow}^q \\
&+ g_{jk,\uparrow}^q (\delta_{jk} - g_{kj,\uparrow}^q) - g_{jj,\uparrow}^q g_{kk,\downarrow}^q - g_{jj,\downarrow}^q g_{kk,\uparrow}^q \\
&+ g_{jj,\downarrow}^q g_{kk,\downarrow}^q + g_{jk,\downarrow}^q (\delta_{jk} - g_{kj,\downarrow}^q)]. \quad (\text{A30})
\end{aligned}$$

The charge compressibility κ is related to charge susceptibility χ_c as $\kappa = \frac{\chi_c}{n_c^2}$ via

$$\chi_c = \frac{\partial n_c}{\partial \mu} = \frac{1}{N_s} \frac{\partial \langle \hat{N}_c \rangle}{\partial \mu} = \frac{1}{N_s T} (\langle \hat{N}_c^2 \rangle - \langle \hat{N}_c \rangle^2), \quad (\text{A31})$$

where total number of c electron $\langle \hat{N}_c \rangle = \sum_{j\sigma} \langle \hat{c}_{j\sigma}^\dagger \hat{c}_{j\sigma} \rangle$ and $\langle \hat{N}_c^2 \rangle$ is given by

$$\begin{aligned}
\langle \hat{N}_c^2 \rangle &= \frac{1}{N_m} \sum_{\{q_j\}} \sum_{j,k,\sigma,\sigma'} \langle\langle (\hat{c}_{j\sigma}^\dagger \hat{c}_{j\sigma}) (\hat{c}_{k\sigma'}^\dagger \hat{c}_{k\sigma'}) \rangle\rangle \\
&= \frac{1}{N_m} \sum_{\{q_j\}} \sum_{j,k} \times [g_{jj,\uparrow}^q g_{kk,\uparrow}^q \\
&+ g_{jk,\uparrow}^q (\delta_{jk} - g_{kj,\uparrow}^q) + g_{jj,\uparrow}^q g_{kk,\downarrow}^q + g_{jj,\downarrow}^q g_{kk,\uparrow}^q \\
&+ g_{jj,\downarrow}^q g_{kk,\downarrow}^q + g_{jk,\downarrow}^q (\delta_{jk} - g_{kj,\downarrow}^q)], \quad (\text{A32})
\end{aligned}$$

which is in fact the charge-charge correlation function/factor structure $C_{\text{SDW}}(\mathbf{q})$ at $\mathbf{q} = 0$.

For calculating dynamic quantities like conductance, (imaginary) time-dependent correlation function such as $\langle\langle \hat{c}_i^\dagger(\tau) \hat{c}_j \rangle\rangle$, $\langle\langle \hat{c}_i(\tau) \hat{c}_j^\dagger \rangle\rangle$ has to be considered. It is easy to show that,

$$\begin{aligned}
\hat{c}_i^\dagger(\tau) &= \sum_n \hat{d}_n^\dagger(\tau) (\phi_n^i)^* = \sum_n \hat{d}_n^\dagger (\phi_n^i)^* e^{\tau E_n(q)} \\
\hat{c}_i(\tau) &= \sum_n \hat{d}_n(\tau) \phi_n^i = \sum_n \hat{d}_n \phi_n^i e^{-\tau E_n(q)}. \quad (\text{A33})
\end{aligned}$$

Therefore,

$$\begin{aligned}
\langle\langle \hat{c}_i^\dagger(\tau) \hat{c}_j \rangle\rangle &= \sum_n f_F(E_n(q)) e^{\tau E_n(q)} (\phi_n^i)^* \phi_n^j \\
\langle\langle \hat{c}_i(\tau) \hat{c}_j^\dagger \rangle\rangle &= \sum_n (1 - f_F(E_n(q))) e^{-\tau E_n(q)} \phi_n^i (\phi_n^j)^* \\
\langle\langle \hat{c}_i^\dagger \hat{c}_j(\tau) \rangle\rangle &= \sum_n f_F(E_n(q)) e^{-\tau E_n(q)} (\phi_n^i)^* \phi_n^j \\
\langle\langle \hat{c}_i \hat{c}_j^\dagger(\tau) \rangle\rangle &= \sum_n (1 - f_F(E_n(q))) e^{\tau E_n(q)} \phi_n^i (\phi_n^j)^*. \quad (\text{A34})
\end{aligned}$$

Using time-dependent correlation function, the imaginary-time Green's function for fixed Ising spin configuration is

$$\begin{aligned}
G_{ij}^q(\tau) &= -\langle\langle T_\tau \hat{c}_i(\tau) \hat{c}_j^\dagger \rangle\rangle \\
&= -\theta(\tau) \langle\langle \hat{c}_i(\tau) \hat{c}_j^\dagger \rangle\rangle + \theta(-\tau) \langle\langle \hat{c}_i^\dagger \hat{c}_j(\tau) \rangle\rangle. \quad (\text{A35})
\end{aligned}$$

Thus, if assuming $\tau > 0$, one finds the following relations between time-dependent correlation functions and their Green's function,

$$\begin{aligned}
G_{ji}^q(-\tau) &= \langle\langle \hat{c}_i^\dagger(\tau) \hat{c}_j \rangle\rangle, G_{ij}^q(\tau) = -\langle\langle \hat{c}_i(\tau) \hat{c}_j^\dagger \rangle\rangle \\
G_{ji}^q(\tau) &= \langle\langle \hat{c}_i^\dagger \hat{c}_j(\tau) \rangle\rangle, G_{ij}^q(-\tau) = -\langle\langle \hat{c}_i \hat{c}_j^\dagger(\tau) \rangle\rangle. \quad (\text{A36})
\end{aligned}$$

The Fourier transformation of $G_{ij}^q(\tau)$ reads

$$G_{ij}^q(\omega_n) = \int_0^\beta d\tau e^{i\omega_n \tau} G_{ij}^q(\tau) = \sum_n \frac{\phi_n^i (\phi_n^j)^*}{i\omega_n - E_n(q)}. \quad (\text{A37})$$

The corresponding retarded Green's function is obtained via analytic continuity $i\omega_n \rightarrow \omega + i0^+$

$$G_{ij}^q(\omega) = \sum_n \frac{\phi_n^i (\phi_n^j)^*}{\omega + i0^+ - E_n(q)}. \quad (\text{A38})$$

And the related spectral function is

$$A_{ij}^q(\omega) = -\frac{1}{\pi} G_{ij}^q(\omega) = \sum_n \phi_n^i (\phi_n^j)^* \delta(\omega - E_n(q)). \quad (\text{A39})$$

The spectral function with momentum-dependence has essential importance to spectral experiments, which can be found as

$$A^q(k, \omega) = \frac{1}{N_s} \sum_{ij} e^{-ik(R_i - R_j)} A_{ij}^q(\omega). \quad (\text{A40})$$

Now, the density of state is found as

$$\begin{aligned}
N(\omega, q) &= -\frac{1}{\pi} \frac{1}{N_s} \sum_j \text{Im} G_{jj}^q(\omega) \\
&= \frac{1}{N_s} \sum_{n,j} \phi_n^j (\phi_n^j)^* \delta(\omega - E_n(q)) \\
&= \frac{1}{N_s} \sum_{n,j} \langle n|j \rangle \langle j|n \rangle \delta(\omega - E_n(q)) \\
&= \frac{1}{N_s} \sum_n \delta(\omega - E_n(q)) \quad (\text{A41})
\end{aligned}$$

which is consistent with previous formalism.

As an application, one can use above formalism to calculate dc conductance as

$$\sigma_{dc} = \lim_{\omega \rightarrow 0} \frac{\text{Im} \Lambda_{xx}(k=0, \omega)}{\omega}, \quad (\text{A42})$$

where the retarded current-current correlation function $\Lambda_{xx}(k=0, \omega)$ can be obtained via its imaginary-time form

$$\Lambda_{xx}(k, i\Omega_n) = \frac{1}{N_s} \sum_{i,j} e^{ik(R_i - R_j)} \int d\tau e^{i\Omega_n \tau} \langle \hat{J}_x(i, \tau) \hat{J}_x(j, 0) \rangle. \quad (\text{A43})$$

Here, \hat{J}_x is x -axis component of current operator. Because our model is defined on a lattice, in terms of Peierls substitution, the external electromagnetic potential $A_x(i) \equiv A_{i,i+x}$ is introduced as

$$-t \sum_{\langle ij \rangle, \sigma} \hat{c}_{i\sigma}^\dagger \hat{c}_{j\sigma} \longrightarrow -t \sum_{\langle ij \rangle, \sigma} e^{ieA_{ij}} \hat{c}_{i\sigma}^\dagger \hat{c}_{j\sigma} \quad (\text{A44})$$

with $A_{ij} = -A_{ji}$. Now, $\hat{J}_x(i)$ is derived as

$$\hat{J}_x(i) = \lim_{A \rightarrow 0} \frac{\delta \hat{H}}{\delta A_x(i)} = ite \sum_{\sigma} (\hat{c}_{i+x, \sigma}^\dagger \hat{c}_{i\sigma} - \hat{c}_{i\sigma}^\dagger \hat{c}_{i+x, \sigma}). \quad (\text{A45})$$

Therefore,

$$\langle \hat{J}_x(i, \tau) \hat{J}_x(j, 0) \rangle = \frac{1}{N_m} \sum_{\{q\}} \langle \langle \hat{J}_x(i, \tau) \hat{J}_x(j, 0) \rangle \rangle \quad (\text{A46})$$

and

$$\begin{aligned} \frac{1}{(ite)^2} \langle \langle \hat{J}_x(i, \tau) \hat{J}_x(j, 0) \rangle \rangle &= \sum_{ij, \sigma, \sigma'} g_{i,i+x, \sigma}^q (g_{j,j+x, \sigma'}^q - g_{j+x, j, \sigma'}^q) \\ &+ g_{i+x, i, \sigma}^q (g_{j+x, j, \sigma'}^q - g_{j, j+x, \sigma'}^q) \\ &- \delta_{\sigma\sigma'} G_{j+x, i, \sigma}^q(-\tau) G_{i+x, j, \sigma}^q(\tau) \\ &+ \delta_{\sigma\sigma'} G_{j, i, \sigma}^q(-\tau) G_{i+x, j+x, \sigma}^q(\tau) \\ &+ \delta_{\sigma\sigma'} G_{j+x, i+x, \sigma}^q(-\tau) G_{i, j, \sigma}^q(\tau) \\ &- \delta_{\sigma\sigma'} G_{j, i+x, \sigma}^q(-\tau) G_{i, j+x, \sigma}^q(\tau). \end{aligned} \quad (\text{A47})$$

Here, $g_{ij\sigma}^q$ has no frequency-dependence and imaginary part, thus it cannot contribute to the conductance and will be neglected hereafter. Integrating over τ gives

$$\begin{aligned} &\int d\tau e^{i\Omega_n \tau} \frac{1}{(ite)^2} \langle \langle \hat{J}_x(i, \tau) \hat{J}_x(j, 0) \rangle \rangle \\ &- T \sum_{\omega_n, \sigma} G_{j+x, i, \sigma}^q(\omega_n) G_{i+x, j, \sigma}^q(\omega_n + \Omega_n) \\ &+ T \sum_{\omega_n, \sigma} G_{j, i, \sigma}^q(\omega_n) G_{i+x, j+x, \sigma}^q(\omega_n + \Omega_n) \\ &+ T \sum_{\omega_n, \sigma} G_{j+x, i+x, \sigma}^q(\omega_n) G_{i, j, \sigma}^q(\omega_n + \Omega_n) \\ &- T \sum_{\omega_n, \sigma} G_{j, i+x, \sigma}^q(\omega_n) G_{i, j+x, \sigma}^q(\omega_n + \Omega_n) \\ &= \sum_{\sigma} \int d\omega_1 \int d\omega_2 \frac{f_F(\omega_1) - f_F(\omega_2)}{i\Omega_n - \omega_2 + \omega_1} \times [-A_{j+x, i, \sigma}^q(\omega_1) A_{i+x, j, \sigma}^q(\omega_2) \\ &+ A_{j, i, \sigma}^q(\omega_1) A_{i+x, j+x, \sigma}^q(\omega_2) + A_{j+x, i+x, \sigma}^q(\omega_1) A_{i, j, \sigma}^q(\omega_2) \\ &- A_{j, i+x, \sigma}^q(\omega_1) A_{i, j+x, \sigma}^q(\omega_2)], \end{aligned} \quad (\text{A48})$$

which leads to the retarded current-current correlation

$$\begin{aligned} \Lambda_{xx}(k, \omega + i0^+) &= \frac{(ite)^2}{N_s N_m} \sum_{\{q\}} \sum_{ij, \sigma} \int d\omega_1 \int d\omega_2 \frac{f_F(\omega_1) - f_F(\omega_2)}{\omega + i0^+ - \omega_2 + \omega_1} \\ &\times e^{ik(R_i - R_j)} [-A_{j+x, i, \sigma}^q(\omega_1) A_{i+x, j, \sigma}^q(\omega_2) + A_{j, i, \sigma}^q(\omega_1) A_{i+x, j+x, \sigma}^q(\omega_2) \\ &+ A_{j+x, i+x, \sigma}^q(\omega_1) A_{i, j, \sigma}^q(\omega_2) - A_{j, i+x, \sigma}^q(\omega_1) A_{i, j+x, \sigma}^q(\omega_2)]. \end{aligned} \quad (\text{A49})$$

Now, it is straightforward to get

$$\begin{aligned} \text{Im} \Lambda_{xx}(0, \omega) &= \frac{\pi t^2 e^2}{N_s N_m} \sum_{\{q\}} \sum_{ij, \sigma} \int d\omega_1 (f_F(\omega_1) - f_F(\omega_1 + \omega)) \\ &\times [-A_{j+x, i, \sigma}^q(\omega_1) A_{i+x, j, \sigma}^q(\omega_1 + \omega) + A_{j, i, \sigma}^q(\omega_1) A_{i+x, j+x, \sigma}^q(\omega_1 + \omega) \\ &+ A_{j+x, i+x, \sigma}^q(\omega_1) A_{i, j, \sigma}^q(\omega_1 + \omega) - A_{j, i+x, \sigma}^q(\omega_1) A_{i, j+x, \sigma}^q(\omega_1 + \omega)]. \end{aligned} \quad (\text{A50})$$

Finally, the dc conductance is found to be

$$\sigma_{dc} = \frac{\pi t^2 e^2}{N_m} \sum_{\{q\}} d\omega \frac{-\partial f_F(\omega)}{\partial \omega} \Phi^q(\omega) \quad (\text{A51})$$

with

$$\begin{aligned} \Phi^q(\omega) &= \frac{1}{N_s} \sum_{ij, \sigma} [-A_{j+x, i, \sigma}^q(\omega) A_{i+x, j, \sigma}^q(\omega) + A_{j, i, \sigma}^q(\omega) A_{i+x, j+x, \sigma}^q(\omega) \\ &+ A_{j+x, i+x, \sigma}^q(\omega) A_{i, j, \sigma}^q(\omega) - A_{j, i+x, \sigma}^q(\omega) A_{i, j+x, \sigma}^q(\omega)]. \end{aligned} \quad (\text{A52})$$

Alternatively, $\Lambda_{xx}(0, i\Omega_n) = \int d\tau e^{i\Omega_n \tau} \langle \hat{J}_x(\tau) \hat{J}_x(0) \rangle$, where

$$\hat{J}_x = e \sum_{k\sigma} v_k^x \hat{c}_{k\sigma}^\dagger \hat{c}_{k\sigma}, v_k^x = \frac{\partial \varepsilon_k}{\partial k_x} = 2t \sin k_x. \quad (\text{A53})$$

Here, \hat{J}_x is zero-frequency current operator, which is derived from its real-space form $\hat{J}_x(i)$ via $\hat{J}_x = \sum_i \hat{J}_x(i)$. It is easy to obtain

$$\begin{aligned} \Lambda_{xx}(0, i\Omega_n) &= -\frac{e^2}{N_s N_m} \sum_{\{q\}} \sum_{k\sigma} (v_k^x)^2 \int d\omega_1 \int d\omega_2 \\ &\frac{f_F(\omega_2) - f_F(\omega_1)}{i\Omega_n - \omega_1 + \omega_2} A_{\sigma}^q(k, \omega_1) A_{\sigma}^q(k, \omega_2) \end{aligned} \quad (\text{A54})$$

and

$$\sigma_{dc} = \frac{\pi e^2}{N_s N_m} \sum_{\{q\}} \sum_{k\sigma} (v_k^x)^2 d\omega \frac{-\partial f_F(\omega)}{\partial \omega} (A_{\sigma}^q(k, \omega))^2. \quad (\text{A55})$$

Furthermore, if we introduce $\varphi(\varepsilon) = \frac{1}{N_s} \sum_k \delta(\varepsilon - \varepsilon_k) (v_k^x)^2$, the above formula can be reduced into

$$\sigma_{dc} = \frac{1}{N_m} \sum_{\{q\}} \left[\pi e^2 \sum_{\sigma} \int d\varepsilon \varphi(\varepsilon) \int d\omega \frac{-\partial f_F(\omega)}{\partial \omega} (A_{\sigma}^q(\varepsilon, \omega))^2 \right]. \quad (\text{A56})$$

Note that $\frac{-\partial f_F(\omega)}{\partial \omega} = \frac{\beta}{4 \cosh^2(\omega/2T)}$, thus we obtain

$$\sigma_{dc} = \frac{1}{N_m} \sum_{\{q\}} \left[\pi e^2 \sum_{\sigma} \int d\varepsilon \varphi(\varepsilon) \int d\omega \frac{\beta (A_{\sigma}^q(\varepsilon, \omega))^2}{4 \cosh^2(\omega/2T)} \right]. \quad (\text{A57})$$

Then, for the paramagnetic situation, we finally get

$$\sigma_{dc} = \frac{1}{N_m} \sum_{\{q\}} \left[2\pi e^2 \int d\varepsilon \varphi(\varepsilon) \int d\omega \frac{\beta (A^q(\varepsilon, \omega))^2}{4 \cosh^2(\omega/2T)} \right], \quad (\text{A58})$$

where $\beta = 1/T$ and such formalism is in fact widely used in Monte Carlo simulation and some approximation techniques such as the DMFT.

For spin dynamics of c electrons, we can extract its information via dynamic spin susceptibility $\chi_{zz}(k, \omega)$, whose imaginary-frequency form is defined as

$$\chi^{zz}(k, \Omega_n) = \frac{1}{N_s N_m} \sum_{\{q\}} \sum_{ij} e^{ik(R_i - R_j)} \int d\tau e^{i\Omega_n \tau} \times \langle \langle T_\tau \hat{s}_i^z(\tau) \hat{s}_j^z \rangle \rangle. \quad (\text{A59})$$

Here, similar to current-current correlation, we find

$$\langle \langle T_\tau \hat{s}_i^z(\tau) \hat{s}_j^z \rangle \rangle = \frac{\theta(\tau)}{4} \sum_{\sigma} (g_{ii,\sigma}^q g_{jj,\sigma}^q - g_{ii,\sigma}^q g_{jj,\bar{\sigma}}^q) - \frac{\theta(\tau)}{4} \sum_{\sigma} G_{ji,\sigma}^q(-\tau) G_{ij,\sigma}^q(\tau). \quad (\text{A60})$$

So, the dynamic spin susceptibility has the following form

$$\chi^{zz}(k, \omega) = \frac{1}{4N_s N_m} \sum_{\{q\}, ij, \sigma} e^{ik(R_i - R_j)} [\delta_{\omega,0} (g_{ii,\sigma}^q g_{jj,\sigma}^q - g_{ii,\sigma}^q g_{jj,\bar{\sigma}}^q) - \int d\omega_1 \int d\omega_2 \frac{f_F(\omega_1) - f_F(\omega_2)}{\omega + i0^+ - \omega_2 + \omega_1} \times A_{ji,\sigma}^q(\omega_1) A_{ij,\sigma}^q(\omega_2)]. \quad (\text{A61})$$

One can also study the transverse spin susceptibility $\chi^{+-}(k, \omega)$ via

$$\chi^{+-}(k, \Omega_n) = \frac{1}{N_s N_m} \sum_{\{q\}, ij} e^{ik(R_i - R_j)} \int d\tau e^{i\Omega_n \tau} \times \langle \langle T_\tau \hat{s}_i^+(\tau) \hat{s}_j^- \rangle \rangle, \quad (\text{A62})$$

where $\langle \langle T_\tau \hat{s}_i^+(\tau) \hat{s}_j^- \rangle \rangle = -\theta(\tau) G_{ji,\uparrow}^q(-\tau) G_{ij,\downarrow}^q(\tau)$. Thus, it is easy to obtain

$$\chi^{+-}(k, \omega) = \frac{-1}{N_s N_m} \sum_{\{q\}, ij} e^{ik(R_i - R_j)} \int d\omega_1 \int d\omega_2 \times \frac{f_F(\omega_1) - f_F(\omega_2)}{\omega + i0^+ - \omega_2 + \omega_1} A_{ji,\uparrow}^q(\omega_1) A_{ij,\downarrow}^q(\omega_2). \quad (\text{A63})$$

Appendix B: phase diagram with compressibility

A similar phase diagram is also elaborated with color-coded compressibility, on both $T - \mu$ and $n_c - T$ plane (see Fig. 10) to provide a more intuitive insight into IKL. The MI state turns out to emerge in a quite small region with Fermi level in band gap. Since in band gap the particle number is not sensitive to the change of chemical potential, the MI region looks much larger in the $T - \mu$ phase diagram. Actually, as shown in Fig. 10 b, the SM behavior sustains within a quite wide range of doping.

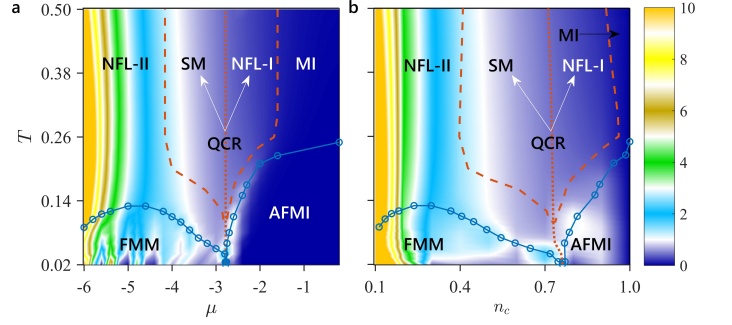


FIG. 10. Phase diagram of the doped IKL in the background of color-coded charge compressibility in (a) $\mu - T$ plane, (b) $n_c - T$ plane. The low temperature regime is divided into an antiferromagnetic insulator (AFMI) and a ferromagnetic metal (FMM) by a first-order transition, which transforms to a weak first-order transition and finally ends at the critical end point (CEP). At high temperature above CEP, a quantum critical region (QCR) is induced by doping-driven Mott insulator-metal transition, which displays the strange metal (SM) behavior in the metallic part. We refer the insulator-like part to the first non-Fermi liquid (NFL-I). Out of QCR, there exists a Mott insulator (MI) at lower doping and the second non-Fermi liquid (NFL-II) at a higher doping.

Appendix C: the separatrix line

In previous DMFT studies of Hubbard model, the 'zero field' trajectory $\mu^*(T)$ (the so-called instability trajectory) is determined as the minimum of curvature of free energy functional, *i.e.*, the so-called 'quantum Widom line'^{11,12}. Actually, it is the center of the corresponding QCR which could separate the metalliclike and insulator-like behaviors. However, this method is no longer feasible in Monte Carlo simulation. Fortunately, the previous theoretical and experimental studies have confirm that the scaling behavior is not sensitive to the choice of $\mu^*(T)$ ¹². Therefore, in this paper we alternatively determine the separatrix by the minimum of error bar with varying doping at a specific temperature in Monte Carlo simulation, to mark the states in equal proximity to both FMM and AFMI. Error bar is an appropriate quantity to determine the separatrix, which has an intrinsic dynamic feature. Since the minimum of error bar infers that the calculated quantity is quite independent of the magnetic configuration, thus it corresponds to the state with no more tendency to either competing phase. We carry out a careful Monte Carlo simulation and reveal the separatrix located at $\mu = -2.76$ (denoted as red dash-dotted line in all plots), which is almost independent upon variation of temperature.

Appendix D: dynamical mean-field analysis

In this section, we cross-check the scaling behavior observed by Monte Carlo simulation with the DMFT. The DMFT we utilized is the single-site DMFT without non-local correlations, which is limited to the paramagnetic region above magnetic phase transition. Although DMFT is an approximate method,

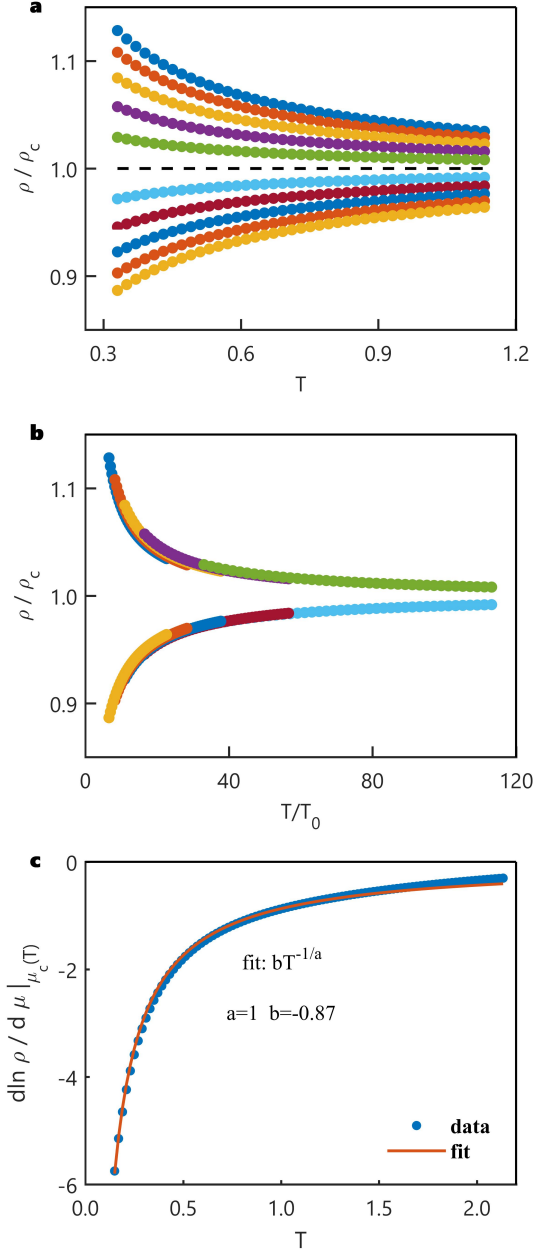


FIG. 11. (a) Resistivity curves calculated by dynamical mean field theory (DMFT), which are plotted along different trajectories $-0.04 \leq \delta\mu \leq +0.04$ with respect to the separatrix line (black dash line). (b) Scaling behavior of resistivity. (c) Derivative of resistivity with respect to μ ($\partial\rho(U, T)/\partial\mu|_{\mu_c}$) along the separatrix line. It fits well to a power-law curve with exponent -1, indicating the scaling formula exponent $z\nu = 1$.

it could still provide a completely nonperturbative description of the strong interaction effect. Its advantage is to offer a clear connection between phenomenon and mechanism. Especially at the high temperature where most non-local correlations are destroyed by thermal fluctuation, the DMFT is quite reliable. Its result could help identifying the effect of insulator-metal

crossover and excluding the influence of magnetic transition. Fortunately, the QCR is just located in the paramagnetic region and could be understood in the framework of DMFT.

In the DMFT analysis, we set the same parameter as the one in Monte Carlo simulation $J = 14$. We report that the results obtained with Monte Carlo simulation and DMFT are qualitatively agree with each other. Firstly, we divide the calculated resistivity by the one along the separatrix line $\rho^*(T)$, and then rescale the temperature with an appropriate parameter in the form of power-law $T_0(\delta\mu) = c|\delta\mu|^{z\nu}$. In Fig. 11(a,b) we plot the scaling behavior of the resistivity curves parallel with the separatrix line. Similar with the result of Monte Carlo simulation, the family of resistivity curves are collapsed onto two branches, which display the characteristic quantum critical scaling within the formula

$$\rho(T, \delta\mu) = \rho^*(T)f(T/T_0(\delta\mu)). \quad (D1)$$

In both branches, the scaling parameter are chosen in the power-law form with the same exponents. The scaling holds in the doping region ($-0.04 \leq \delta\mu \leq 0.04$), which is very small due to the strong correlation. Besides, we note that a perfect mirror symmetry is revealed at all parameter, and the resistivity curve along the separatrix line just corresponds to $\partial \log \rho^*(T)/\partial\mu = 0$. As the analysis in previous studies¹², the authors providing a smart method to evaluate the exponent, *i.e.*, in the systems with such remarkable mirror symmetry the resistivity curve along the separatrix could be fitting with exponent $z\nu$ as

$$\frac{\partial \log \rho^*(\mu, T)}{\partial \mu} \propto T^{-\frac{1}{z\nu}}. \quad (D2)$$

With this formula, we display a perfect fitting behavior in Fig. 11(c) and it do cover a quite large temperature scale. The exponent is fitted as $z\nu = 1$, which is applied in Fig. 11(c). The critical exponent in the DMFT $z\nu = 1$ indicates the scaling behavior might belong to the classical Ising universality class. What's more, the low temperature magnetic transition emanated from the CEP also displays the standard classical liquid-gas universality class. This Ising scaling could be understood in the way that the phase diagram is mainly divided to two magnetic states, *i.e.*, the FM one and the AFM one, and these two dominant phases as two whole parts compete with each other. Thus it leads to kinds of Ising like criticality through entire parameter region.

Appendix E: Magnetic states at low temperature

1. Magnetic states

In previous studies about the half-filling IKL²³, we confirm the theorem proved by Kennedy and Lieb³¹ with Monte Carlo simulation, *i.e.*, the ground state configuration $\{q_i\}$ has the twofold degenerated checkerboard order $q_j = \pm(-1)^j$. In this paper, we report that not only for half-filling situation, at any doping level the IKL system always has magnetic ordered ground state. Besides, due to the strong longitudinal Kondo

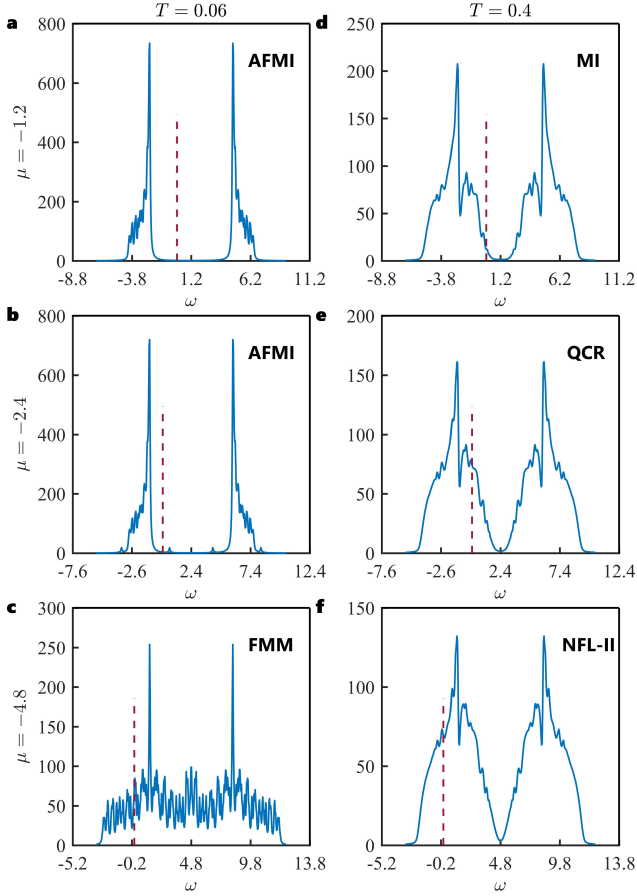


FIG. 12. Density of states (DOS) in low temperature regions (left panel, $T = 0.06$) and high temperature regions (right panel, $T = 0.4$). Position of Fermi level is marked with right dashed line.

coupling, c electrons construct the same magnetism with local moments. In this section, we will illustrate the mechanism of each states and analyze transition properties between different states.

At the left side of CEP, the $\{q_i\}$ has Néel AFM configuration. Around half-filling situation, IKL is a MI with AFM order. With increasing doping, there is a crossover to normal AFMI state. Further increasing doping holes leads to FMM state, when across the CEP to its right side. We confirm different magnetic structures with significant structure factor in Brillouin zone. The insulating and metallic states are confirmed by behavior of DOS and resistivity. In the left panel of Fig. 12 we demonstrate the DOS at different doping level. The zero DOS ($\omega = 0$) at small doping and finite DOS ($\omega = 0$) at large doping suggest a transition from insulator to metal. AFMI is characterized by a fully open gap and increasing resistivity with decreasing temperature. In FMM state, it instead has finite DOS ($\omega = 0$) and the resistivity decreases with decreasing temperature. In Fig. 12c (left panel), the clear quasiparticle peak suggests a FL-like behavior. Even at metallic state ($\mu = -5, -6$) resistivity still has an upward tendency at sufficiently low temperature, which is attributed to the weak localization property of a two-dimensional system.

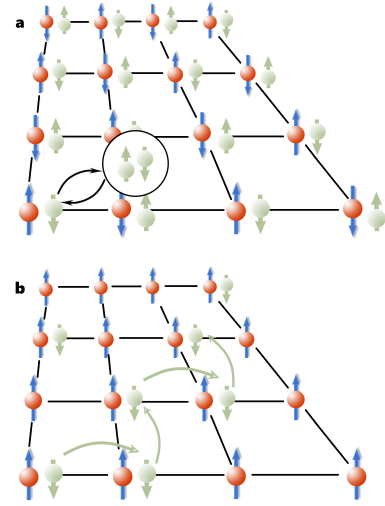


FIG. 13. Schematic explanation of the magnetic structure at different doping levels. f -electrons are denoted by the red balls, and itinerant electrons are denoted by the green balls. (a) Around half filling, antiferromagnetic (AFM) configuration permits the virtual hopping of c electrons, leading to delocalization with lowered kinetic energy $E_0^{(2)} \sim -t_c^2/J$. In the ferromagnetic (FM) background, the virtual hopping is instead forbidden by the Pauli exclusion principle. (b) Away from half filling, FM configuration could enhance the conductivity of c -electrons, where c -electrons could freely move in the FM background without the charge of energy elevation. To the contrary, electron movement would be hindered in the AFM configuration, since the spin orientations of c -electron and its neighbor local moments are parallel to each other and thus hopping will greatly enhance the energy ($\Delta E \sim J$).

The mechanism of different magnetism at small and large doping is illustrated in Fig. 13, respectively. Under strong interaction, Kondo coupling term could be taken as the zero-order Hamiltonian while hopping term is merely taken as perturbation. Due to strong correlation, double occupation would significantly elevate the energy and give the energy change $\Delta E \sim J$, thus c electrons can hardly move on lattice. Therefore, around half-filling the ground state is insulating, where c electrons localized at each site ($n_c \lesssim 1$). The tendency to antiferromagnetism with increasing doping can be understood under the framework of perturbation theory. In antiferromagnetism the process of virtual hopping of c electrons leads to delocalization and thus decreases the kinetic energy ($E_0^{(2)} \sim -t_c^2/J$, see Fig. 13 a). This mechanism is similar with the one in half-filled Hubbard model³². As to large doping, the lattice is away from half-filling and hopping of c electrons is no longer forbidden. Thus the charge transport would be hindered by the presence of AFM background, whereas the FM background can greatly enhance the conductivity. (In the AFM background, spin of c electron would be antiparallel to the on-site local moment, whereas parallel to the nearest neighbor local moment.) Thus with increasing doping the delocalization of c electrons occurs together with a magnetic structure transformation, leading to a FMM state.

Actually, before approaching the AFMI-FMM phase tran-

sition, the competition between different magnetic structures is already present and leads to spin excitations. In Fig. 14 we display the DOS around the transition in AFMI state. When exceeding a critical doping (around $\mu = -2.2$), a bound state emerges in the fully opened Mott gap. The bound state is caused by the domain wall excitation of AFM configuration in the parameter region away from half-filling. It is the lead-up to the magnetic phase transition.

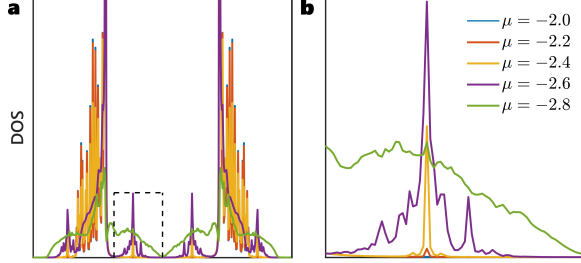


FIG. 14. DOS calculated at $T = 0.06$ at different level of doping. For clarity, we adjust the x -axis ω to unify the location of gap in different curves.

2. Magnetic phase transition

The transition property of IKL is complicated, which combines the competing between both metal-insulator and AFM-FM structures. As shown in the main text, at ground state the AFM-FM transition occurs around $\mu_c = -2.76$ is a strong first-order phase transition (marked by a blue solid circle). In Fig. 15 we plot the finite-size scaling behavior of checkerboard order parameter ϕ_c to investigate the transition properties. In a small doping region ($-2.80 \leq \mu \leq -2.74$), the checkerboard order parameter and the c -electron density ($n_c \sim 0.76$) are almost invariant (see Fig. 15a). This suggests a strong first-order phase transition located along a coexistence dome, which includes the spin density wave states with $(0, 0)$, (π, π) , $(\pi, 0)$, $(0, \pi)$ order. The coexistence regime would be much larger under a weak correlation. Increasing temperature leads to a weak first-order phase transition. In Fig. 15b,c the finite-size scaling behavior, which is belonging to the two-dimensional Ising universality class, indicates a weak first-order phase transition. This phase transition finally terminates at the CEP ($T = 0.06$, $\mu = -2.76$). Further increasing the temperature, a metal-insulator crossover occurs instead (see Fig. 13 (d)).

Appendix F: non-Fermi liquid states at high temperature

As shown in Fig. 10, there are four different states at high temperature: MI, NFL-I, SM and NFL-II. With increasing temperature, an obvious transformation of DOS occurs with the thermally driven magnetic-paramagnetic phase transition.

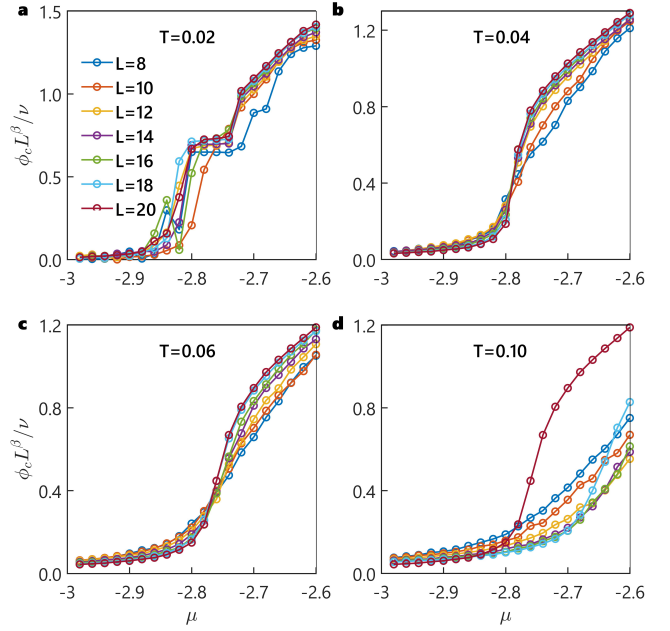


FIG. 15. Finite-size scaling behavior of checkerboard order parameter ϕ_c for different temperature (a) $T = 0.02$, (b) $T = 0.04$, (c) $T = 0.06$, (d) $T = 0.10$. At sufficiently low temperature (a), the flat order parameter suggests a first-order phase transition, along with the coexistent region of antiferromagnetism and ferromagnetism. The crossing of the different system size at T_c reveals a scaling behavior belongs to a 2D Ising universality class at (b,c), suggesting a weak first-order phase transition. At higher temperature (d), the scaling behavior vanishes, instead indicating a crossover or phase transition in higher order.

At high temperature, the two-peaked spectral function is robust (see the right panel of Fig. 12). Due to strong coupling, most paramagnetic region of doped IKL displays robust NFL behavior, which is indicated by the violation of Luttinger's theorem.

We refer the insulator-like part of QCR to the NFL-I. In Fig. 16 we demonstrate the anomalous transport and thermodynamics of the NFL-I state ($\mu = -2.0$). In NFL-I, the capacity heat displays an obvious $T^{3/2}$ -dependence, which is out of the FL paradigm. As shown in the main text, the resistivity curves display unconventional quantum scaling behavior. However, the insulating properties dominate in a quite large temperature region and thus the resistivity cannot be well scaled by T^α .

In Fig. 17 we demonstrate the anomalous transport and thermodynamics of the NFL-II, which is referred to the large doping regime out of QCR. In the NFL-II a linear- T resistivity is revealed. We distinguish the NFL-II from SM by the absence of both quantum critical scaling behavior and logarithmic temperature dependence of the specific-heat coefficient.

Appendix G: Evolution of Fermi surface

In this section, we analysis the Mott-like band structure and the evolution of Fermi surface under varying doping, to

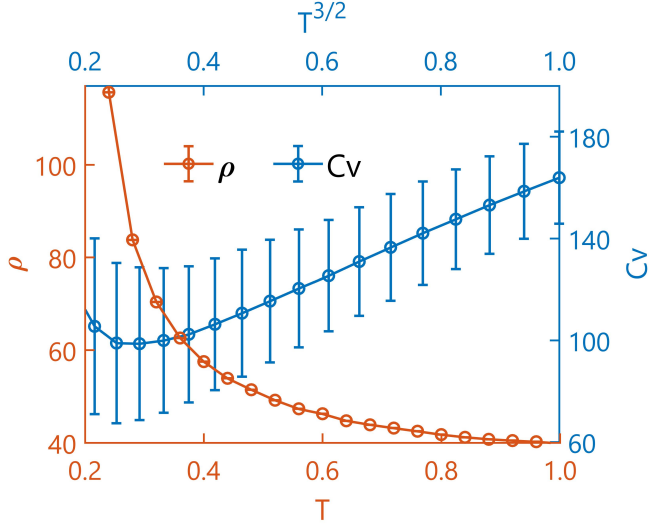


FIG. 16. Anomalous transport and thermodynamics in the first non-Fermi liquid state (NFL-I, $\mu = -2.0$), which is the insulator-like part of the QCR. Specific heat (orange) displays a $T^{3/2}$ -dependence at high temperature region, which is out of the FL paradigm. The resistivity (blue) increases with decreasing temperature, indicating an insulator-like transport properties.

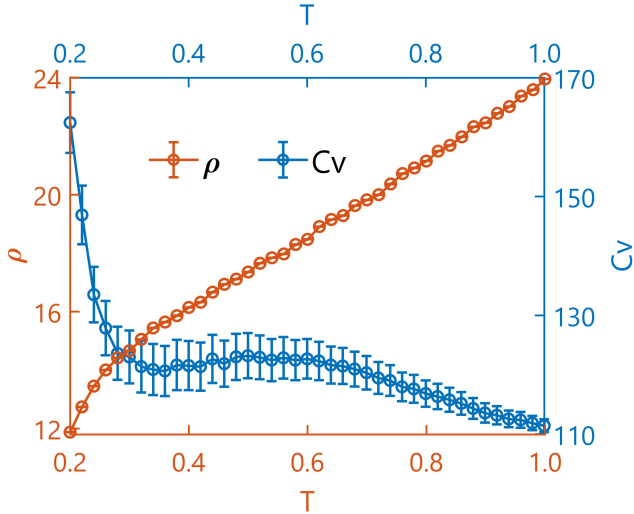


FIG. 17. Anomalous transport and thermodynamics in the second non-Fermi liquid state (NFL-II, $\mu = -4.6$), which is the high temperature region out of the QCR. The resistivity (blue) displays a obvious linear- T dependence.

understand the breaking of Luttinger rule observed in most parameter regime. Although in IKL upper band and lower band do form due to strong interaction, actually the mechanism of the breaking of Luttinger rule is quite different from the one in Hubbard model, where a small Fermi surface emerges for counting only the electrons on the upper band. Besides, remarkable difference of evolution of Fermi surface are observed

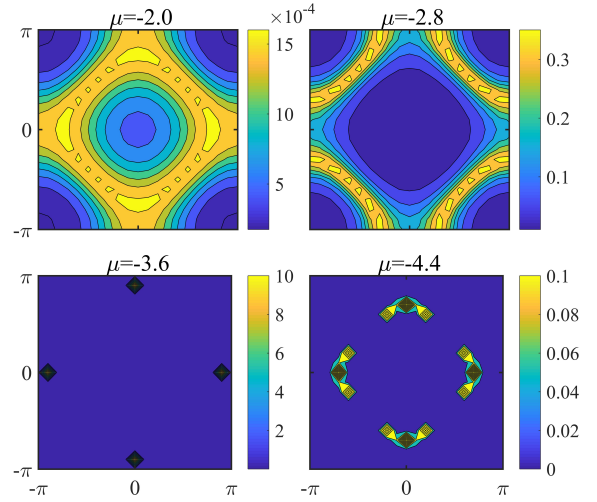


FIG. 18. Spectral function at Fermi energy $A_k(\omega = 0)$ plotted at low temperature ($T = 0.06$) for different doping. High/low density corresponds to the yellow/blue color. Fermi surface contour is denoted by yellow regime. At small doping ($\mu = -2.0$, AFMI state), there is almost no finite spectral function in the entire Brillouin zone with Fermi energy located at the Mott gap. Around the critical $\mu_c = -2.76$, there is a reconstruction of Fermi surface. Further increasing doping leads to a FL-like behavior in FMM state.

at both high and low temperature.

1. low temperature situation

In Fig. 18, we display the evolution of Fermi surface with varying doping at low temperature, where the magnetic structure changes from AFMI to FMM. The situation of magnetic regime is quite different with the paramagnetic one.

In the AFMI even with varying doping around half-filling, the Fermi energy is located within the Mott gap. In this specific case, the spectral function is almost zero in the entire Brillouin zone (see the upper panel of Fig. 18). In fact, the FMM is a FL-like state with well-defined Fermi surface. With increasing doping, there is a reconstruction of Fermi surface around magnetic phase transition ($\mu_c = -2.8$). We report that this reconstruction of Fermi surface is caused by the competition between local and itinerant properties. The Fermi then changes from a square to a diamond shape. The Luttinger theorem is abided in FMM, where the spectral function has merely the contribution of one spin (see lower panel of Fig. 18).

2. high temperature situation

In Fig. 19 we display the spectral weight with increasing doping, to study the evolution of Fermi surface at high temperature. With doping, the size of Fermi surface smoothly decreases with several crossovers. From MI to QCR states, and finally to the NFL-II state, no jump in Fermi surface is observed. Note that the size of Fermi surface is anomalously

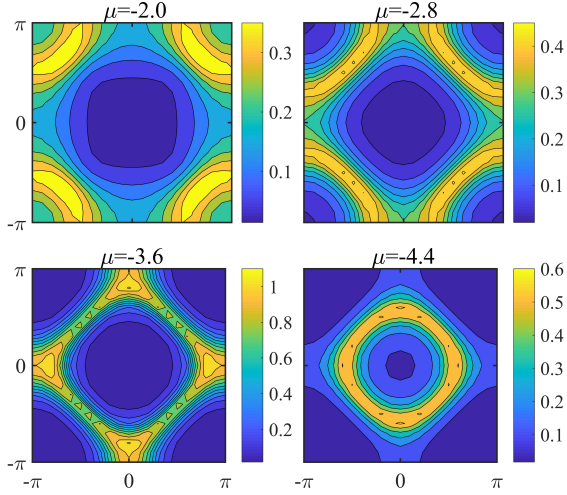


FIG. 19. Spectral function at Fermi energy $A_k(\omega = 0)$ plotted at high temperature ($T = 0.4$) for different doping. High/low density corresponds to the yellow/blue color. Fermi surface contour is denoted by yellow regime. With increasing doping, the Fermi surface volume smoothly decreases, which corresponds merely to the electron occupation of the lower band.

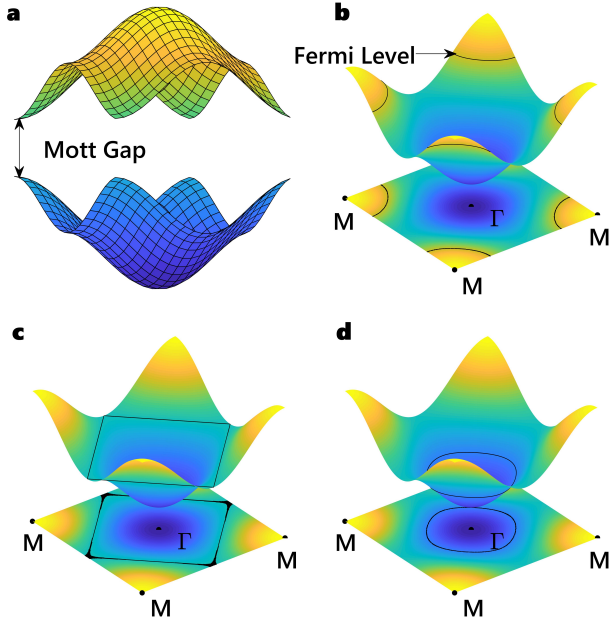


FIG. 20. **a** Schematic representation of entire band structure of IKL, where the single particle band in free system splits to an upper band and a lower band under strong correlation. **b,c,d** Schematic representation of lower band and its projection on the Fermi level. The intersection between the lower band and Fermi level is denoted by black line. With increasing doping, the Fermi surface transforms from a diamond shape to a square shape and at last a circle shape.

larger than the area encompassed by Luttinger contour.

In Hubbard model, the Mott phase with doping electrons around half-filling has a well-known small Fermi surface. Although the Luttinger rule is not satisfied, the Luttinger count is exactly corresponding to the density of electrons with the formula $IL = n - 1$ ¹⁸. The so-called small Fermi surface merely encompasses the states occupied in upper band, thus leads to a smaller Fermi surface and also a smaller Luttinger volume, which is quite different from the behavior of doped IKL observed in this paper.

This origination of derivation is more similar with the one in the doped MI of Hastugai-Kohmoto (HK) model³⁰. In HK model, the $\hat{c}_{k\sigma}$ is not the elementary excitation, thus both the upper and lower bands have non-zero spectral weight in the singly occupied situation. Therefore, once we counting the electron density as the number of occupied states in k -space, a strong deviation would emerge for neglecting the fact that spectral weight for each state is no longer equal one. Thus in the MI state near half-filling, the Luttinger rule anomalously suggests $n_c \sim 2$. The present study reasserts that Luttinger rule could merely cover some specific systems, in which electron excitation can be taken as elementary excitation.

In this paper we try to attribute this deviation to the specific band structure of IKL. As shown in Fig. 20 (a), the strong interaction opens a significant Mott gap and constructs a two-band structure, corresponding to the singlet and triplet states, respectively. At half filling, the Fermi energy is located within the spectral gap and thus leads to the MI state. This MI state could be destroyed by doping enough holes/electrons, *i.e.*, tuning the chemical potential μ . When μ approaches the lower/upper band, the system transform from MI to some metallic states. In MI, the Luttinger volume covers the total Brillouin zone, thus $IL \sim 2 \times n_c$ ($IL = 2, n_c = 1$). As shown in the main text, at most hole doping situation the Luttinger count also deviates as $IL \sim 2 \times n_c$. We argue that the violation of Luttinger's theorem is induced by the overlook of upper band, where the Fermi surface plotted with spectral weight merely reflects the occupied states in the lower band. Thus the weight of states is double counted in the lower band. To test this argument, we demonstrate the intersection between the lower band and Fermi energy in Fig. 20. With increasing doping, the shape of intersection transforms in the same way with Fermi surface, which changes from a diamond shape (Fig. 20 (b)) with small doping to a square shape (Fig. 20 (c)) at intermediate doping and finally a circle (Fig. 20 (d)) with large doping.

Appendix H: Hubbard-I approximation

In the paramagnetic MI, one can follow the Hubbard-I approximation to give a rough solution for MI itself. To this purpose, we use the equation of motion (EOM) formalism and define the retarded Green's function as

$$G_{i,j,\sigma}(\omega) = \langle\langle \hat{c}_{i\sigma} | \hat{c}_{j\sigma}^\dagger \rangle\rangle. \quad (\text{H1})$$

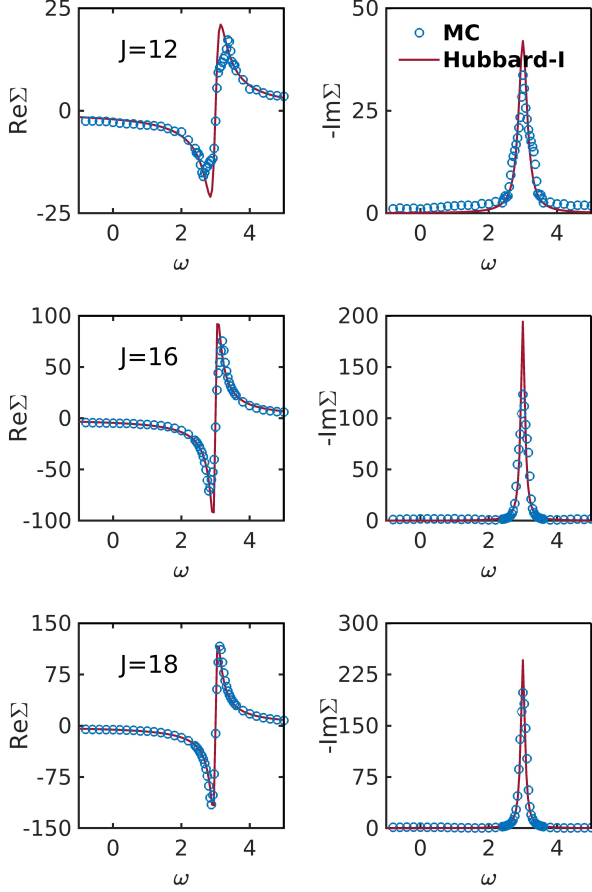


FIG. 21. Frequency dependence of self-energy ($\mu = -3.0, T = 1.0$) for different coupling strength, including $J = 12$ (upper panel), $J = 16$ (middle panel) and $J = 18$ (lower panel). The result of Hubbard I approximation valid at strong coupling limit is displayed (red line), and it is in good agreement with MC result (blue circle).

By using the standard EOM relation,

$$\omega \langle \langle \hat{A} | \hat{B} \rangle \rangle_{\omega} = \langle [\hat{A}, \hat{B}]_{+} \rangle + \langle \langle [\hat{A}, \hat{H}]_{-} | \hat{B} \rangle \rangle_{\omega}. \quad (\text{H2})$$

For IKL, it follows that

$$\omega \langle \langle \hat{c}_{i\sigma} | \hat{c}_{j\sigma}^{\dagger} \rangle \rangle_{\omega} = \delta_{ij} - t \Delta_{im} \langle \langle \hat{c}_{m\sigma} | \hat{c}_{j\sigma}^{\dagger} \rangle \rangle_{\omega} + \frac{J}{2} \sigma \langle \langle \hat{S}_i^z \hat{c}_{i\sigma} | \hat{c}_{j\sigma}^{\dagger} \rangle \rangle_{\omega}. \quad (\text{H3})$$

Here, Δ_{im} denotes m is the nearest-neighbor site of i . For $\langle \langle \hat{S}_i^z \hat{c}_{i\sigma} | \hat{c}_{j\sigma}^{\dagger} \rangle \rangle_{\omega}$, we have

$$\langle \langle \hat{S}_i^z \hat{c}_{i\sigma} | \hat{c}_{j\sigma}^{\dagger} \rangle \rangle_{\omega} = \langle \hat{S}_i^z \rangle \delta_{ij} - t \Delta_{il} \langle \langle \hat{S}_l^z \hat{c}_{l\sigma} | \hat{c}_{j\sigma}^{\dagger} \rangle \rangle_{\omega} + \frac{J}{8} \langle \langle \hat{c}_{i\sigma} | \hat{c}_{j\sigma}^{\dagger} \rangle \rangle_{\omega}. \quad (\text{H4})$$

If no further EOM is involved, to close EOM we have to decouple $\langle \langle \hat{S}_i^z \hat{c}_{l\sigma} | \hat{c}_{j\sigma}^{\dagger} \rangle \rangle_{\omega}$ as

$$\langle \langle \hat{S}_i^z \hat{c}_{l\sigma} | \hat{c}_{j\sigma}^{\dagger} \rangle \rangle_{\omega} \simeq \langle \hat{S}_i^z \rangle \langle \langle \hat{c}_{l\sigma} | \hat{c}_{j\sigma}^{\dagger} \rangle \rangle_{\omega}. \quad (\text{H5})$$

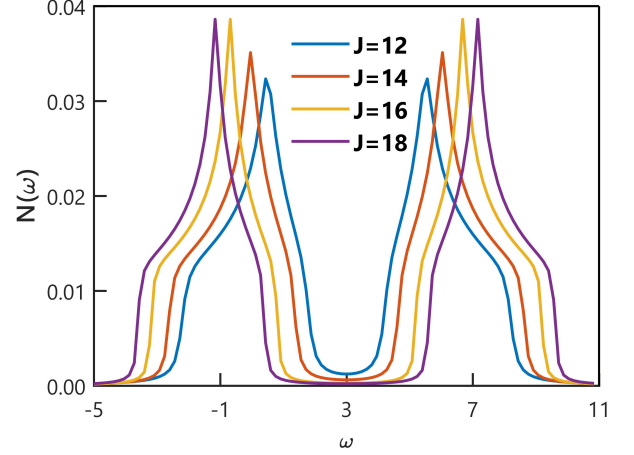


FIG. 22. DOS $N(\omega)$ of c -electron in SM state with Hubbard-I approximation ($\mu = -3.0$), indicating robust two-peaked feature of spectral function as Monte Carlo simulation.

In paramagnetic strong coupling regime, there is no finite magnetic order, thus $\langle \hat{S}_i^z \rangle = 0$. Meanwhile, the contribution from $\langle \langle \hat{S}_i^z \hat{c}_{i\sigma} | \hat{c}_{j\sigma}^{\dagger} \rangle \rangle_{\omega}$ vanishes due to the decoupling and the above equation has a complete solution:

$$\left(\omega - \frac{J^2}{16\omega} \right) \langle \langle \hat{c}_{i\sigma} | \hat{c}_{j\sigma}^{\dagger} \rangle \rangle_{\omega} = \delta_{ij} - t \Delta_{im} \langle \langle \hat{c}_{m\sigma} | \hat{c}_{j\sigma}^{\dagger} \rangle \rangle_{\omega}, \quad (\text{H6})$$

which can be written as

$$\left(\omega - \frac{J^2}{16\omega} \right) G_{i,j,\sigma}(\omega) = \delta_{ij} - t \Delta_{im} G_{m,j,\sigma}(\omega). \quad (\text{H7})$$

Now, performing the Fourier transformation

$$G_{i,j,\sigma}(\omega) = \frac{1}{N_s} \sum_k e^{ik(R_i - R_j)} G_{\sigma}(k, \omega), \quad (\text{H8})$$

we have

$$\sum_k \left(\omega - \frac{J^2}{16\omega} \right) G_{\sigma}(k, \omega) e^{ik(R_i - R_j)} = \sum_k e^{ik(R_i - R_j)} \left(\omega - \frac{J^2}{16\omega} \right) G_{\sigma}(k, \omega) - t \Delta_{im} G_{\sigma}(k, \omega) e^{ik(R_m - R_j + R_i - R_i)}. \quad (\text{H9})$$

Here, $-t \Delta_{im} e^{ik(R_m - R_i)} = -t \sum_{\delta} \delta e^{-ik\delta} = \varepsilon_k$ and we have $\sum_k [(\omega - \frac{J^2}{16\omega}) G_{\sigma}(k, \omega) - 1] e^{ik(R_i - R_j)} = 0$, which gives the single-particle Green's function as

$$G_{\sigma}(k, \omega) = \frac{1}{\omega - \frac{J^2}{16\omega} - \varepsilon_k} = \frac{\alpha_k^2}{\omega - \hat{E}_k^+} + \frac{1 - \alpha_k^2}{\omega - \hat{E}_k^-}. \quad (\text{H10})$$

Here, the coherent factor $\alpha_k^2 = \frac{1}{2} \left(1 + \frac{\varepsilon_k}{\sqrt{\varepsilon_k^2 + J^2/4}} \right)$ and

$$\hat{E}_k^{\pm} = \frac{1}{2} \left[\varepsilon_k \pm \sqrt{\varepsilon_k^2 + J^2/4} \right]. \quad (\text{H11})$$

When chemical potential μ is considered explicitly, the Hamiltonian reads

$$\hat{H} = -t \sum_{i,j\sigma} \hat{c}_{i\sigma}^\dagger \hat{c}_{j\sigma} + \frac{J}{2} \sum_{j\sigma} \hat{S}_j^z \sigma \hat{c}_{j\sigma}^\dagger \hat{c}_{j\sigma} - \mu \sum_{j\sigma} \hat{c}_{j\sigma}^\dagger \hat{c}_{j\sigma}. \quad (\text{H12})$$

The effect of μ can be included easily by setting ω to $\omega + \mu$ and we have

$$G_\sigma(k, \omega) = \frac{1}{\omega + \mu - \frac{J^2}{16(\omega + \mu)} - \varepsilon_k}. \quad (\text{H13})$$

And the self-energy function is found to be $\Sigma(\omega) = \frac{J^2}{16(\omega + \mu)}$, which is real.

Therefore, although no SDW state appears, the band of conduction electron has been split into two Hubbard-like bands. This is driven by the local Kondo interaction and the resulting

state is MI if half-filling is satisfied. Moreover, the DOS in the present Hubbard-I approximation can be obtained by

$$N(\omega) = \frac{1}{N_s} \sum_{k\sigma} \left[-\frac{1}{\pi} \text{Im} G_\sigma(k, \omega + i\Gamma) \right], \quad (\text{H14})$$

where Γ is the damping factor.

Here we also provide the frequency dependence of self-energy for different coupling strength in Fig. 21 ($\mu = -3.0$, and $J = 12, J = 16, J = 18$). The Hubbard-I approximation works well especially at strong coupling situation. With the fitting coefficient provided in main text, we plot the DOS in Fig. 22, which displays a robust two-peaked feature as Monte Carlo simulation. We argue that the robust two-peaked spectral function and the T-independent scattering rate conspire to construct the linear- T resistivity in doped IKL.

* zhongy@lzu.edu.cn

- 1 P. A. Lee, N. Nagaosa, and X.-G. Wen, *Rev. Mod. Phys.* **78**, 17 (2006).
- 2 G. R. Stewart, *Rev. Mod. Phys.* **83**, 1589 (2011).
- 3 B. J. Powell and R. H. McKenzie, *Reports on Progress in Physics* **74**, 056501 (2011).
- 4 B. Shen, Y. Zhang, Y. Komijani, M. Nicklas, R. Borth, A. Wang, Y. Chen, Z. Nie, R. Li, X. Lu, and et al., *Nature* **579**, 51 (2020).
- 5 R. Daou, N. Doiron-Leyraud, D. LeBoeuf, S. Li, F. Laliberté, O. Cyr-Choiniere, Y. Jo, L. Balicas, J.-Q. Yan, J.-S. Zhou, *et al.*, *Nature Physics* **5**, 31 (2009).
- 6 A. Legros, S. Benhabib, W. Tabis, F. Laliberté, M. Dion, M. Lizaire, B. Vignolle, D. Vignolles, H. Raffy, Z. Li, *et al.*, *Nature Physics* **15**, 142 (2019).
- 7 F. Kagawa, K. Miyagawa, and K. Kanoda, *Nature* **436**, 534 (2005).
- 8 H. Oike, K. Miyagawa, H. Taniguchi, and K. Kanoda, *Phys. Rev. Lett.* **114**, 067002 (2015).
- 9 S. S. P. Parkin, E. M. Engler, R. R. Schumaker, R. Lagier, V. Y. Lee, J. C. Scott, and R. L. Greene, *Phys. Rev. Lett.* **50**, 270 (1983).
- 10 J. Bruin, H. Sakai, R. Perry, and A. Mackenzie, *Science* **339**, 804 (2013).
- 11 J. Vučićević, D. Tanasković, M. J. Rozenberg, and V. Dobrosavljević, *Phys. Rev. Lett.* **114**, 246402 (2015).
- 12 J. Vučićević, H. Terletska, D. Tanasković, and V. Dobrosavljević, *Phys. Rev. B* **88**, 075143 (2013).
- 13 A. Georges, G. Kotliar, W. Krauth, and M. J. Rozenberg, *Rev. Mod. Phys.* **68**, 13 (1996).
- 14 G. Kotliar, S. Y. Savrasov, K. Haule, V. S. Oudovenko, O. Parcollet, and C. A. Marianetti, *Rev. Mod. Phys.* **78**, 865 (2006).
- 15 P. Limelette, A. Georges, D. Jérôme, P. Wzietek, P. Metcalf, and J. Honig, *Science* **302**, 89 (2003).
- 16 M. Krzyzosiak, R. Gonczarek, and A. Gonczarek, *Journal of Physics: Conference Series* **152**, 012058 (2009).
- 17 L. Landau, *Soviet Physics JETP-USSR* **3**, 920 (1957).
- 18 I. Osborne, T. Paiva, and N. Trivedi, “Fermi-surface reconstruction in the repulsive fermi-hubbard model,” (2020), arXiv:2001.07197 [cond-mat.str-el].
- 19 E. W. Huang, R. Sheppard, B. Moritz, and T. P. Devereaux, *Science* **366**, 987 (2019).
- 20 S. Tsuda, C. L. Yang, Y. Shimura, K. Umeo, H. Fukuoka, Y. Yamane, T. Onimaru, T. Takabatake, N. Kikugawa, T. Terashima, H. T. Hirose, S. Uji, S. Kittaka, and T. Sakakibara, *Phys. Rev. B* **98**, 155147 (2018).
- 21 J. Shin, Z. Schlesinger, and B. S. Shastry, *Phys. Rev. B* **95**, 205140 (2017).
- 22 A. E. Sikkema, W. J. L. Buyers, I. Affleck, and J. Gan, *Phys. Rev. B* **54**, 9322 (1996).
- 23 W.-W. Yang, J. Zhao, H.-G. Luo, and Y. Zhong, *Phys. Rev. B* **100**, 045148 (2019).
- 24 In this paper we determine the separatrix by the minimum of error bar with varying doping at a specific temperature in Monte Carlo simulation, see details in the supplementary materials.
- 25 The character of NFL-I and NFL-II are demonstrated in detail in the supplementary materials.
- 26 The critical exponent for c -electron ($(z\nu)_c = 1.25$) is different from the one of f -electron ($(z\nu)_f = 0.55$).
- 27 I. Dzyaloshinskii, *Phys. Rev. B* **68**, 085113 (2003).
- 28 J. M. Luttinger, *Phys. Rev.* **119**, 1153 (1960).
- 29 P. Cha, A. A. Patel, E. Gull, and E.-A. Kim, *Phys. Rev. Research* **2**, 033434 (2020).
- 30 P. W. Phillips, L. Yeo, and E. W. Huang, *Nature Physics* (2020), 10.1038/s41567-020-0988-4.
- 31 T. Kennedy and E. H. Lieb, *Physica A: Statistical Mechanics and its Applications* **138**, 320 (1986).
- 32 D. I. Khomskii, *Basic aspects of the quantum theory of solids: order and elementary excitations* (Cambridge University Press, 2010).